

Magnetic Signatures of a Putative Fractional Topological Insulator in Twisted MoTe₂

Yiping Wang^{1,2,*}, Gillian E. Minarik^{1,*}, Weijie Li³, Yves Kwan⁴, Shuai Yuan³, Eric Anderson³, Chaowei Hu⁵, Julian Ingham⁶, Jeongheon Choe¹, Takashi Taniguchi⁷, Kenji Watanabe⁸, Xavier Roy¹, Jiun-Haw Chu⁵, Raquel Queiroz⁶, James C. Hone², N. Regnault^{9,10,11}, Xiaodong Xu^{3,5}, and Xiaoyang Zhu^{1,†}

¹ Department of Chemistry, Columbia University, New York, NY 10027, USA

² Department of Mechanical Engineering, Columbia University, New York, NY 10027, USA

³ Department of Physics, University of Washington, Seattle, WA 98195, USA

⁴ Department of Physics, University of Texas at Dallas, Richardson, TX 75080, USA

⁵ Department of Materials Science and Engineering, University of Washington, Seattle, WA 98195, USA

⁶ Department of Physics, Columbia University, New York, NY 10027, USA

⁷ Research Center for Materials Nanoarchitectonics, National Institute for Materials Science, 1-1 Namiki, Tsukuba 305-0044, Japan

⁸ Research Center for Electronic and Optical Materials, National Institute for Materials Science, 1-1 Namiki, Tsukuba 305-0044, Japan

⁹ Center for Computational Quantum Physics, Flatiron Institute, 162 5th Avenue, New York, NY 10010, USA

¹⁰ Department of Physics, Princeton University, Princeton, New Jersey 08544, USA

¹¹ Laboratoire de Physique de l'Ecole Normale Supérieure, PSL University, CNRS, Sorbonne Universités, Université Paris Diderot, Sorbonne Paris Cité, Paris, France

The interplay among electronic correlation, topology, and time-reversal-symmetry (TRS) often leads to exotic quantum states of matter. Primary examples include the recently realized fractional Chern insulators (FCIs) in twisted MoTe₂ bilayers (tMoTe₂)¹⁻⁴ and multilayer graphene aligned with hBN⁵, where TRS is broken in partially filled flat moiré Chern bands. Among the FCIs in tMoTe₂, the most robust is at a hole filling of $\nu = -2/3$ per moiré unit cell^{1-4,6,7}. Interestingly, transient optical sensing⁸ and more recent transport measurements^{9,10} revealed a correlated state at $\nu = -4/3$, twice the filling factor for the $\nu = -2/3$ FCI. Here, employing pump-probe circular dichroism (CD) measurements on tMoTe₂

* These authors contributed equally.

† To whom correspondence should be addressed. Email: xyzhu@columbia.edu

with twist angles $\theta = 3.9^\circ$ and 3.7° , we find that the $\nu = -4/3$ state exhibits vanishing magnetization ($m = 0$) in finite windows of out-of-plane magnetic field $|\mu_0 H| \leq \sim 2\text{-}4$ mT, and a first order phase transition to $\pm m$ states at higher fields. This out-of-plane antiferromagnetic (AFM) like behavior is notably absent for all other correlated states and disappears for the $\nu = -4/3$ state at higher or lower twist angles of $\theta = 4.0^\circ$ and 3.3° . The observed magnetic signature at $\nu = -4/3$ is consistent with a predicted fractional topological insulator (FTI) with TRS, consisting of two copies of -2/3 FCIs with opposite chiralities¹¹. We support these findings with calculations in the interacting continuum model of tMoTe₂. Our work presents a candidate for fractional topological insulators with TRS¹²⁻¹⁴.

We investigate four dual-gated MoTe₂ bilayer devices (D1-4) with twist angles $\theta = 3.90 \pm 0.06^\circ$ (D1), $3.70 \pm 0.07^\circ$ (D2), $4.00 \pm 0.08^\circ$ (D3), and $3.30 \pm 0.07^\circ$ (D4). Devices at $3.6^\circ \leq \theta \leq 4.0^\circ$ are known to host the robust $\nu = -2/3$ FCI state¹⁻⁴. Device fabrication and characterization are detailed in the appendix (Methods, Extended Data Fig. 1), and in a previous report⁹. We have developed a pump-probe time-domain approach, Fig. 1a, to probe moiré quantum phases^{15,16} and demonstrated its superior sensitivity in detecting a large number of correlated states, including incipient states, in the tMoTe₂ system⁸. A reflectance spectrum is characterized by derivative shape across a resonance, Fig. 1b. Transient reflectance monitors $\Delta R/R_0$, where $\Delta R = R(\Delta t) - R_0$; $R(\Delta t)$ and R_0 are the reflectance spectrum at the pump-probe delay of Δt and without pump, respectively. The extraordinary sensitivity of this method lies in its background free nature when the pump pulse selectively targets the correlation gap or pseudo gap (Methods). We note that the results presented in the following are independent of pump light polarization, consistent with non-selective melting driven by excitation across the correlation gaps (Extended Data Fig. 2)⁸. The pump-induced closing of correlation gaps or pseudo gaps results in increases in effective dielectric constant and the Pauli blocking effect, as detailed below, leading to a decrease in sensor exciton oscillator strength shown as the characteristic flip in sign in $\Delta R/R_0$ (Fig. 1b, bottom).

Here we implement the approach in transient CD to quantify the spin/valley polarization based on optical selection rules for exciton-Fermi polarons^{17,18}. An attractive polaron (AP) consists of an exciton in the K^+ (K^-) valley bound to carriers in the opposite K^- (K^+) valley. Due to spin-valley locking, the transition is selectively probed by σ^+ (σ^-) circularly polarized light and this approach has been applied to the static sensing of spin/valley polarization in the region of spontaneous TRS

breaking, including Chern insulators, in tMoTe₂.^{19,20} At $\sim 0.4 \leq |v| \leq 1.3$, the AP transition emerges for only one circular polarization because the hole population resides entirely in one valley ($0.4 \leq |v| \leq 1$) or is highly polarized towards one valley ($1 < |v| \leq 1.3$).^{1-4,20,21}

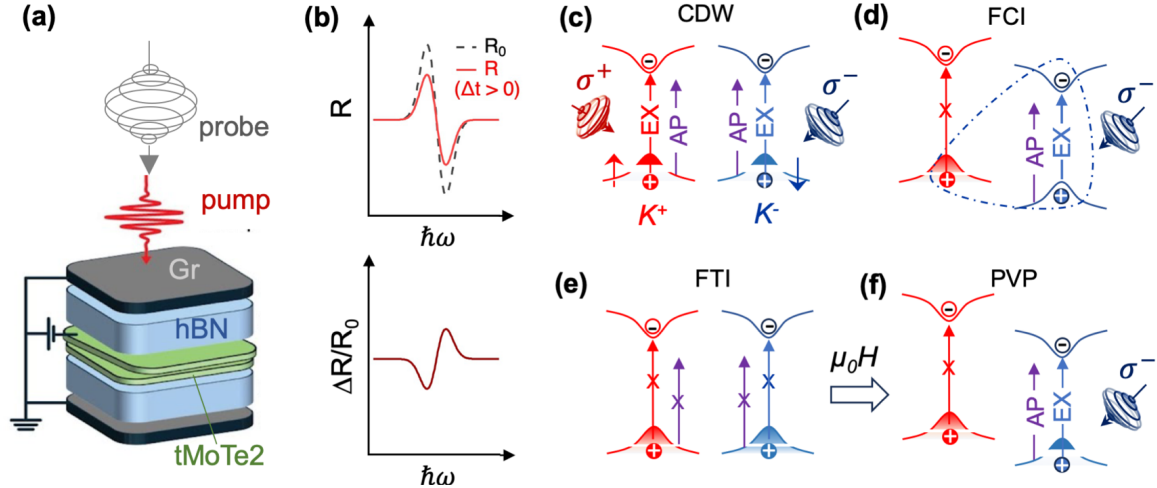


Figure 1. Transient circular dichroism (tCD) probes spin valley polarization. (a) Illustration of the tCD experiment on dual-gated tMoTe₂ devices. A pump pulse with photon energy below the semiconductor band gap selectively disrupts correlated states in tMoTe₂. A probe pulse with circular polarization (σ^+ or σ^-) determines reflectance (R) at the exciton and trion resonances; (b) Illustration of an exciton (EX) or attractive polaron (AP) reflectance spectrum (R_0 and R before and after the arrival of pump pulse, respectively), with pump-induced change ($\Delta R/R_0$) shown in the lower panel; (c) Optical transitions of a CDW state where gap opening in both K^+ and K^- valleys partially restores EX and AP transitions for σ^+ and σ^- probes; (d) optical transitions of an FCI state with polarization in the K^+ valley, where EX and AP transitions are active in the K^- valley with σ^- probe, while the EX transition in the K^+ valley by the σ^+ probe is inhibited due to Pauli blocking; (e) tCD of a proposed FTI state where hole populations in both K^+ and K^- valleys inhibits EX and AP transitions for either σ^+ or σ^- probe; (f) tCD of a partially valley polarized (PVP) state resulting from the breaking of TRS by an external magnetic field (B) partially restores EX and AP transitions in the K^- valley with σ^- probe. Note that, in (d) and (f), the roles of σ^+ and σ^- probes are reversed when the K^- valley is polarized.

We first illustrate the transient optical sensing of charge density waves (CDWs), sometimes called generalized Wigner crystals, that yield $\Delta R/R_0$ contrasts much stronger than FCIs do⁸. At a high carrier doping level, excitonic transitions occurring in the presence of charge carriers in the same valley are expected to be suppressed due to Pauli blocking²². However, the formation of a CDW state splits the band into sub-bands due to translational symmetry breaking, the lowest of which becomes completely filled, leaving a lower effective density in the remaining partially filled sub-bands. Consequently, the opening of a CDW gap can enhance and sharpen exciton/AP transitions in both K^+ and K^- valleys involving the sub-band without carrier population, i.e., a partial alleviation of Pauli blocking, Fig. 1c. For comparison, the Chern gaps are generally smaller

than CDW gaps in the tMoTe₂ system⁸. The critical temperature of the $\nu = -2/3$ FCI state in tMoTe₂ is $T_c \sim 2\text{-}4$ K.^{1-3,19} As detailed in Methods, while the nominal temperature reading of our sample stage is 1.6 K, the actual sample temperature during spectroscopic measurements is likely higher. The closeness to T_c means that the FCI states probed here are likely incipient and the Chern gaps not fully formed. As a result, excitonic transitions for probes can be suppressed (red arrow) due to Pauli blocking in the K^+ valley but allowed for the K^- valley.

By contrast, we now consider exciton and AP sensing for the candidate FTI in tMoTe₂ at $\nu = -4/3$, consisting of two copies of FCIs at $\nu = -2/3$ in K^+ and K^- valleys¹¹. Hole populations are present in both K^+ and K^- valleys with small or pseudo Chern gaps. Pauli blocking may remain effective and diminish exciton/AP transitions for both σ^+ and σ^- polarized probes (Fig. 1e). If the TRS of the proposed FTI is broken by an external magnetic field to form a partially valley polarized (PVP) state - where the hole fillings are $\nu^+ = -1$ and $\nu^- = -1/3$ in the K^+ and K^- valley respectively (Fig. 1f) - then σ^+ (σ^-) probes are expected to exhibit different signatures. In such a PVP state, the $\nu^+ = -1$ prohibits σ^+ probe, while $\nu^- = -1/3$ allows σ^- transitions; these distinct spectral signatures are observed in experiments

We first present transient reflectance spectra as a function of ν with σ^+ (Fig. 2a) and σ^- (Fig. 2b) circularly polarized probe light on device D1 ($\theta = 3.9^\circ$), without external magnetic fields ($\mu_0H = 0$ mT). While we resolve correlated states with either σ^+ or σ^- probe polarizations, the spectral amplitudes are different, as expected from the different transition strengths in the presence of spin/valley polarization. In the doping region $-1.3 < \nu < -0.4$, the AP resonance ($\sim 1.2\text{-}1.3$ eV) from σ^+ (Fig. 2a) is stronger than that from σ^- (Fig. 2b) because it is polarized in the K^- valley (negative μ_0H field training). We show in Fig. 2c the difference spectra (Fig. 2c), $|\sigma^+\rangle - |\sigma^-\rangle$, which we take as a proxy to CD. The CD spectra show non-zero intensity only in the region $-1.3 < \nu < -0.4$, where spontaneous spin/valley polarization is known to occur^{1-4,20,21}. While the states are not well-resolved for either σ^+ or σ^- polarization, they are more obvious in the CD spectra, clearly showing the integer and fractional Chern insulators at $\nu = -1$ and $-2/3$, respectively. Interestingly, the transient CD spectra also reveal states slight above or below $\nu \sim -1$; the natures of these states are not known and deserve future investigations. In the following, we focus on the $\nu = -3/2$ and $-4/3$ states that have been detected in transient optical sensing⁸ and confirmed in transport^{9,10,21}. The $\nu = -3/2$ and $\nu = -4/3$ states show distinct signatures in transient spectral sensing.

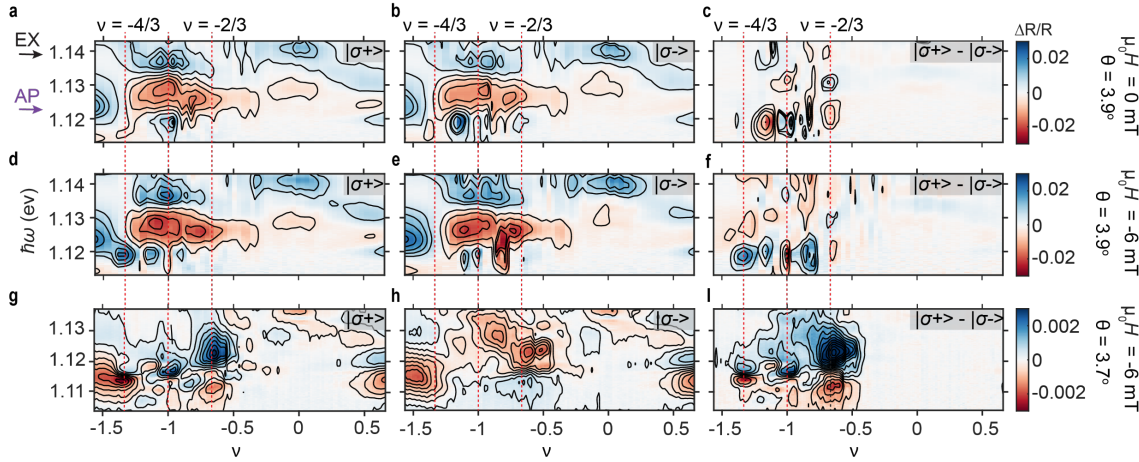


Fig. 2. Transient circular dichroism (CD) reveals distinct spectral signatures for the $v = -4/3$ state. Spectrally resolved transient reflectance maps as a function of moiré filling factor (v) for tMoTe₂ devices D1 ($\theta = 3.9^\circ$, a-f) and D2 ($\theta = 3.7^\circ$, g-i) at external magnetic fields of $\mu_0 H = 0$ (a-c) and $\mu_0 H = -6$ mT (d-i). The left and middle columns are $\Delta R/R$ spectra obtained with probe polarizations of σ^+ and σ^- , respectively, while the right column presents the difference spectra between the two probe polarizations, ($\sigma^+ - \sigma^-$) as proxy to CD spectra. The red-dashed lines mark filling factors of $v = -4/3, -1, -2/3$. All spectra obtained at sample stage temperature of $T = 1.6$ K and a pump-probe delay of $\Delta t = 1.2$ ns.

For $v = -3/2$, we observe the AP resonance with either σ^+ and σ^- polarizations, Fig. 2a and Fig. 2b, suggesting the Pauli blocking effect is suppressed, as expected for a CDW state (see Fig. 1d). Similar behaviors are observed for exciton and AP sensing of other CDW states at $v > -0.4$, including a large number of states on the electron doping side⁸ (see Extended Data Fig. 3). These states are non-magnetic, evident by the vanishing CD signal.

In contrast to the CDWs, the Pauli blocking effect is operative for either σ^+ or σ^- for the $v = -4/3$ state, as evidenced by much weaker signal in spectral regions for both exciton and AP transitions. This observation suggests that, unlike $v = -3/2$ and other CDW states, the $v = -4/3$ state is not a CDW. The -4/3 state also shows zero intensity in CD spectra at zero magnetic field, Fig. 2c, confirming the absence of spontaneous ferromagnetism^{1-4,20,21}. When we add a small out-of-plane magnetic field of $\mu_0 H = -6$ mT to sample D1, Figs. 2d-f, a new signature emerges: we observe a strong AP resonance at $v = -4/3$ for σ^+ polarization (Figs. 2d), but not for σ^- polarization (Fig. 2e). This reveals that hole population is polarized to the K^- valley upon the application of -6 mT magnetic field. Figure 2f now shows that the CD signal of the $v = -4/3$ state is comparable to those in the $-1.3 < v < -0.4$ doping region. Thus, small magnetic field switches the $v = -4/3$ state from

one with no magnetization to a PVP state. In stark contrast, the switching behavior is absent for all other correlated states, including $v = -3/2$. The unique property of the $v = -4/3$ state is reproduced in device D2 ($\theta = 3.7^\circ$) (see Figs. 2g-i).

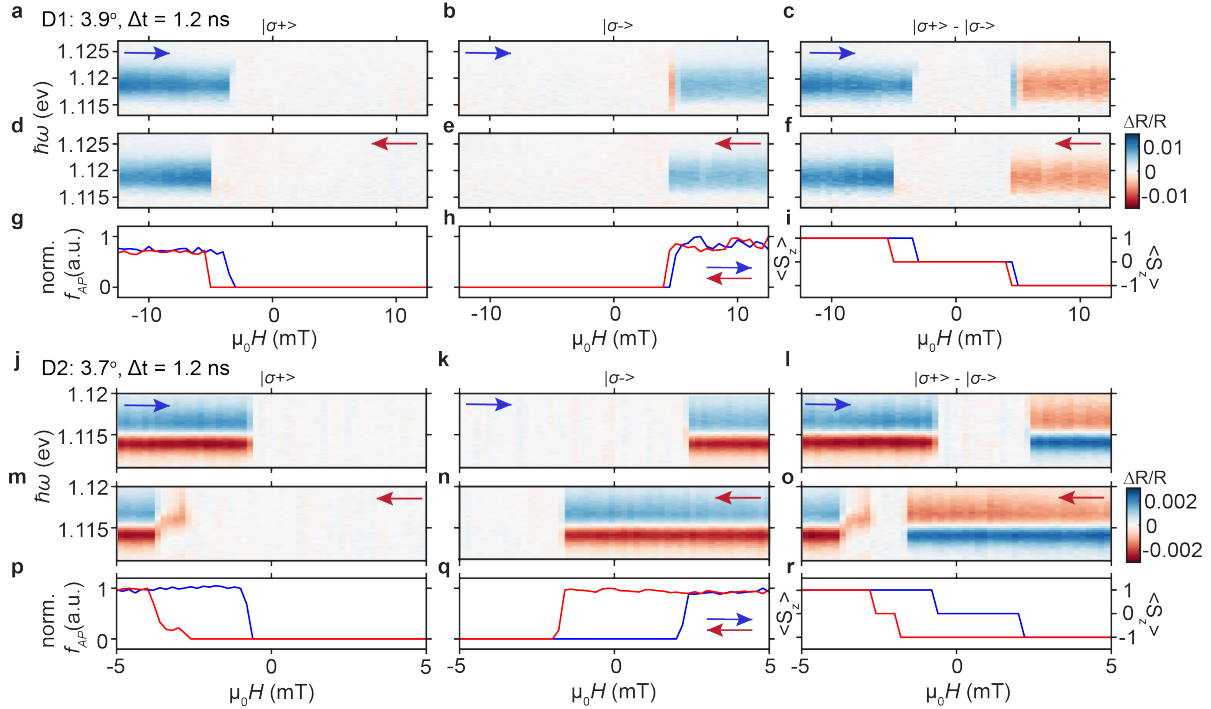


Fig 3. AFM-like magnetic response of the $v = -4/3$ state. a-i Device D1 ($\theta = 3.9^\circ$). Transient reflectance spectra (colored scale $\Delta R/R$) under forward magnetic field sweep probed by a) σ^+ , b) σ^- , and c) $\sigma^+ - \sigma^-$ and backward magnetic field sweep probed by d) σ^+ , e) σ^- , and f) $\sigma^+ - \sigma^-$. AP oscillator strength f_{AP}^\pm extracted from the $\Delta R/R$ spectra under forward (blue) and backward (red) magnetic field sweeps probed by g) σ^+ , h) σ^- polarizations, and i) the corresponding valley/spin polarizations $\langle S_z \rangle = (f_{AP}^+ - f_{AP}^-)/(f_{AP}^+ + f_{AP}^-)$. j-r) Similar data to a-i) for device D2 ($\theta = 3.7^\circ$). Attractive polaron oscillator strengths are extracted from modeling the 2D optical susceptibility described in Methods. All data obtained at $\Delta t = 1.2$ ns and nominal sample stage temperature $T = 1.6$ K.

The magnetic behavior of the $v = -4/3$ state is established in μ_0H -field scans. We present transient reflectance spectra as a function of μ_0H with σ^+ and σ^- polarized probes for devices D1 ($\theta = 3.9^\circ$, Figs. 3a-i) and D2 ($\theta = 3.7^\circ$, Figs. 3j-r) at the fixed filling factor of $v = -4/3$. We first focus on D1. Starting from $\mu_0H = -12$ mT and moving to positive values (Fig. 3a), we observe strong AP resonance from σ^+ polarization, indicating holes predominantly in the polarized K -valley. As the μ_0H field reaches a critical value of ~ -3 mT, we observe a sudden disappearance of the AP resonance, suggesting a first-order phase transition to a state where the same AP transition is forbidden. While the σ^+ -AP transition remains forbidden as μ_0H is further increased to positive

values, the σ^- -AP transition is abruptly switched on for $\mu_0H \geq 5$ mT, Fig. 3b, indicating holes predominantly polarized in the K^+ valley. At $-3 \text{ mT} < \mu_0H < 5 \text{ mT}$, both σ^+ and σ^- AP transitions are inhibited, suggesting both K^+ and K^- valleys are equally populated. The presence of the three states is most obvious in the CD spectra $|\sigma^+ \rangle - |\sigma^- \rangle$, Fig. 3c, which reveals a K^- polarized state on the negative μ_0H side, an intermediate state with equal K^- and K^+ occupations, and a K^+ polarized state on the positive μ_0H side. These three states are also observed as the direction of the μ_0H field sweep is reversed, Figs. 3d-f. The forward and backward μ_0H -sweeps show clear hysteresis, as expected from magnetic transitions.

We extract the AP oscillator strength, f_{AP}^+ and f_{AP}^- for σ^+ and σ^- polarized light from modeling the 2D optical susceptibility (see Methods). We show f_{AP}^+ (Fig. 3g) and f_{AP}^- (Fig. 3h) and the corresponding valley/spin polarizations $\langle S_z \rangle = f_{AP}^+ - f_{AP}^- / (f_{AP}^+ + f_{AP}^-)$ (Fig. 2i). While the hysteresis in the magnetic field sweep for σ^+ (Fig. 3g) or σ^- (Fig. 3h) selectively probes the polarization of the K^- or K^+ valley, $\langle S_z \rangle$ reveals the transitions from K^- polarized, K^- and K^+ equally populated, and K^+ polarized states. The transition near the critical field is hysteretic and sharp, typical for a spin-flip transition. The above magnetic behavior resembles an anti-ferromagnetic (AFM) state under the application of magnetic field along the easy axis.

The flatness of the zero-magnetization region with applied μ_0H field, i.e., zero magnetic susceptibility, suggests the $v = -4/3$ state is gapped in each valley, consistent with the resistive behavior observed in transport measurements^{9,10}. For comparison, CD becomes measurable around $\mu_0H = 0$ mT when the AFM-like behavior disappears at higher temperature (device D1, $\theta = 3.9^\circ$, $T = 6$ K) or smaller twist angle (device D4, $\theta = 3.3^\circ$, $T = 1.6$ K); see below. As shown in Extended Data Fig. 4, the magnetization of the spin/valley polarized states in Fig. 3i at $|\mu_0H| \geq 5$ mT remains constant at external magnetic field as high as $|\mu_0H| = 6$ T, confirming that further hole population transfers are not possible. The saturation behavior suggests that these states are PVPs with $v^+ (v^-) = -1$ in the $K^+ (K^-)$ valley and $v^- (v^+) = -1/3$ in the $K^- (K^+)$ valley.

The observed magnetic behavior is confirmed in μ_0H -field scans on device D2 ($\theta = 3.7^\circ$), Figs. 3j-r. In this device, the $v = -4/3$ state again exhibits zero magnetization in a finite μ_0H field window around 0 mT, switching to positive/negative magnetization outside the window. In each scan direction (Fig. 3j,k or Fig. 3m,n), we observe the transitions from a K^- polarized state to an intermediate state with equal K^- and K^+ occupation, and a K^+ polarized state on the positive μ_0H

side. For either σ^+ or σ^- probe, we observe hysteresis in the two μ_0H -field scan directions, as shown by AP oscillator strength, f_{AP}^\pm , in Fig. 3p, 3q. The magnetic behavior is summarized in the valley spin polarizations $\langle S_z \rangle$, Fig. 3r. The asymmetry in the forward and backward μ_0H -field scans for device D2 may result from a small residual magnetic field at the sample. Except for the sharp transitions, the $\Delta R/R$ signal remains flat, indicating zero magnetic susceptibility.

In both D1 and D2, the AFM-like signature persists at all measured time delays (up to $\Delta t = 1.2$ ns) with identical switching fields, varying only in $\Delta R/R$ intensity (Extended Data Fig 5). This further confirms that the observed AFM-like behavior at $v = -4/3$ is repeatable and intrinsic to the doped moiré devices, rather than a transient light-induced effect. In light of recent work^{23–25}, we rule out optical switching of the Chern number by using the optical power four orders of magnitude below the switching threshold (Methods).

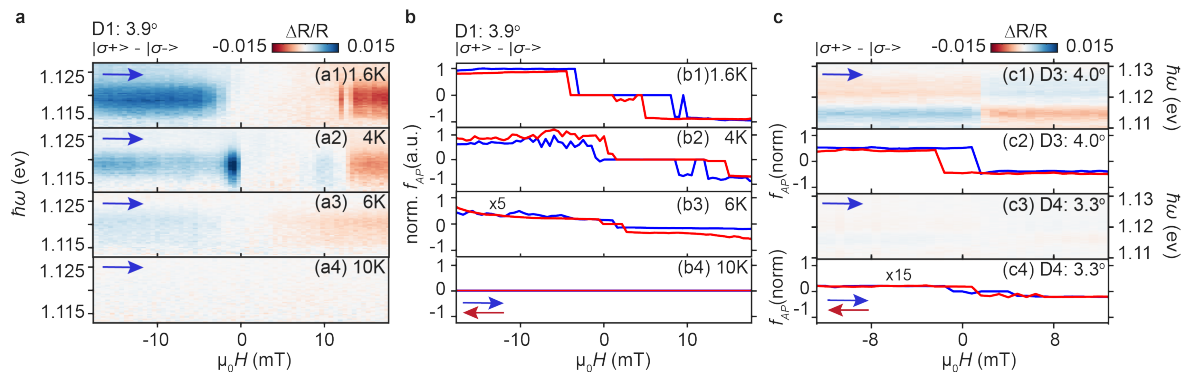


Fig. 4. Temperature and twist angle dependences in the magnetic behavior of the $v = -4/3$ state. a) CD color maps ($\sigma^+ - \sigma^-$) for the forward sweeping magnetic field at $T = 1.6, 4, 6$, and 10 K (a1-4). Signal has notably disappeared at 10 K . b) corresponding CD in AP oscillator strength, ($\sigma^+ - \sigma^-$), at the four temperatures: $T = 1.6, 4, 6$, and 10 K (b1-4). Note that CD in AP oscillator strength in panel (b3) has been multiplied by a factor of 5; c) CD color maps ($\sigma^+ - \sigma^-$) for the forward sweeping magnetic field and the corresponding AP oscillator strength for devices D3 ($\theta = 4.0^\circ$) and D4 ($\theta = 3.3^\circ$) at $T = 1.6\text{ K}$. The hysteresis profiles become ferromagnetic at $\theta = 4.0^\circ$ and paramagnetic at $\theta = 3.3^\circ$. Note the CD in AP oscillator strength has been multiplied by a factor of 15. All transient spectra obtained at $\Delta t = 1.2\text{ ns}$.

We carry out temperature (T) dependent measurements to establish the thermal stability of the AFM-like state for device D1 ($\theta = 3.9^\circ$). Fig. 4a shows transient reflectance spectra for σ^+ probe at the four indicated temperatures, $T = 1.6, 4, 6$, and 10 K ; the corresponding spectra for σ^- probe can be found in Extended Data Fig. 6. We also show the extracted AP oscillator strength, f_{AP}^\pm , in Fig. 2b. While the AFM-like behavior is robust at $T = 1.6\text{ K}$, it becomes unstable from spin fluctuations at $T = 4\text{ K}$ and vanishes at $T = 6\text{ K}$ and 10 K . Thus, the critical temperature for the

AFM-like state at $v = -4/3$ is $T_c \sim 4$ K. We also determine the stability of the observed state with vertical displacement field and find the critical field for destroying the state to be of the order of $E_c \sim 0.1$ V/nm (Extended Data Fig. 7). Both T_c and E_c for the AFM-like state are similar to those for the stability of the $v = -2/3$ FCI at similar twist angles^{1–4,20,21}.

The AFM-like state at $v = -4/3$ appears to exist in a small twist angle range. The magnetic behavior observed at $\theta = 3.7^\circ$ or 3.9° disappears in $\mu_0 H$ -scans at lower or higher twist angles, $\theta = 3.3^\circ$ (D3) and $\theta = 4.0^\circ$ (D4). At $\theta = 4.0^\circ$, Fig. 4b, the magnetic field scan reveals a ferromagnetic state, i.e., the boundary of spontaneous TRS breaking nominally observed for $-1.3 \leq v \leq -0.4$ is extended to $v = -4/3$ - a property which has eluded detection in static optical sensing. Thus, the AFM-like $v = -4/3$ state emerges at the boundaries of other competing orders. At $\theta = 3.3^\circ$, Fig. 4a, there is no evidence for magnetic order for external magnetic fields as high as 6 T (Extended Data Fig. 8). Note that the magnetic field scans in AP oscillator strength for D1 at 6 K (Fig. 4b3) and D4 at 1.6 K (Fig. 4c4) show weak paramagnetic behavior, in contrast to the flat zero CD around zero field in Fig. 3.

We now consider the FTI interpretation of the $v = -4/3$ state in tMoTe₂¹¹. The FTI, which is considered equivalent to the fractional quantum spin Hall (FQSH) effect in 2D, has been the subject of considerable theoretical interest^{26–29}, yet its experimental realization has remained elusive. The most attractive proposal to obtaining FTIs comes from the interacting lattice model where two copies of FCIs with opposite chirality combine to form an FTI with necessary time-reversal symmetry^{12–14}. In view of discoveries of FCIs in topological moiré flat-bands^{1–5,30}, one naturally asks the question on whether FTIs also exist in these systems. Kang et al.³¹ assigned a $v = -3$ state in tMoTe₂ at a relatively small twist angle of $\theta = 2.1^\circ$ to a FQSH state in the second moiré band and this interpretation has attracted considerable theoretical interest^{11,32–39}. However, this state is ferromagnetic, breaks TRS, and shows finite R_{xy} in Hall measurement at zero magnetic field^{21,40,41}.

In contrast, an FTI at $v = -4/3$ preserving TRS can form from two known FCIs at $v = -2/3$ with opposite chirality in tMoTe₂¹¹, as has long been proposed in the interacting lattice model^{12–14}. Such an FTI is predicted to exist only in a small twist angle range around $\theta \sim 3.7^\circ$ ¹¹ consistent with our experimental observations. The presence of two opposite chirality copies of the $v = -2/3$ FCIs preserves TRS, which can be broken by an out-of-plane magnetic field to switch to a PVP

state with $v = -1$ and $-1/3$ in the two K^+/K^- valleys. This leads to an AFM→FM like spin-flip magnetic transition under the application of a weak magnetic field, as is observed here for $\theta = 3.9^\circ$ and 3.7° (Fig. 2 and 3). As mentioned above, the critical temperature and electrical fields of the observed magnetic behavior of the $-4/3$ state are similar to those of the $-2/3$ FCI state, further supporting its origin as two copies of $-2/3$ states with opposite chirality.

We note that the $v = -2$ state in tMoTe₂ is believed to be a quantum spin Hall (QSH) state³¹. However, a similar TRS breaking under weak magnetic field is not expected to occur because both K^+ and K^- valleys are fully occupied in the first moiré band. This is confirmed in our experiment: the $v = -2$ state in D1 (3.9°) exhibits vanishing CD within the range ± 50 mT (Extended Data Fig. 9). Only when Zeeman-field-induced band-crossing occurs between the first Chern band in one valley (K^+ or K^-) and the second Chern band in the opposite can a magnetic switching occur for the QSH at $v = -2$, at $\mu_0 H$ field as high as ~ 14 T and ~ 7 T in tMoTe₂ at $\theta = 3.8^\circ$ and 2.6° , respectively²¹.

Before we present exact diagonalization (ED) calculations, we consider alternative explanations for the AFM-like behavior. We first eliminate the possibility of an inter-valley coherent (IVC) in-plane AFM order, which has been predicted for twisted transitional metal dichalcogenide homobilayers⁴². The IVC state corresponds to an AFM with an in-plane magnetic moments that cant gradually towards the out-of-plane direction in an applied field - in stark contrast to the first-order transitions we observe. Next, we consider the possibility of charge ordered states with out-of-plane AFM order. The most abundant quantum phases in TMD moiré systems are charge orders, often referred to as CDWs, as is also shown in the tMoTe₂ system⁸. However, the AFM-like magnetic behavior observed here for the $v = -4/3$ state is distinct from those of all other CDW states in the tMoTe₂ system. Specifically, at zero field, exciton and AP features remain weak for both σ^+ and σ^- polarized probes at $v = -4/3$, implying Pauli blocking remains effective in both valleys - unlike the CDW case, where the formation of mini bands due to translational symmetry breaking alleviates the effect of Pauli blocking.

To further support the FTI interpretations, we carry out ED calculations at $v = -4/3$ on the continuum model of tMoTe₂ (Fig. 5a, see Method section 8.1) for $\theta = 3.4^\circ$ - 4.4° . In Fig. 5b, we plot the energy difference (ΔE) between the ground states in the PVP ($v^+ = -1$ and $v^- = -1/3$) and non-polarized ($v^+ = -2/3$ and $v^- = -2/3$) sectors on a 12-site lattice. The computational complexity

requires projection to the lowest valence band, but we still incorporate crucial band-mixing effects⁴³⁻⁴⁵ by allowing a restricted number of holes N^1_{\max} to occupy the second valence band (labelled band1 in Fig. 5b). While the PVP sector has lower energy in the absence of band-mixing, increasing N^1_{\max} can lead to a transition to the non-polarized sector. The energy difference remains small (fraction of meV), signaling the extremely close competition between the valley sectors, as is reflected in the small critical magnetic fields in switching between the states in Fig. 3. Calculations on other system sizes (see Method section 8.2) reveal similar qualitative behaviors, though finite-size effects preclude a more quantitative analysis. We also find an analogous depolarizing effect of band-mixing at $v = -3/2$ (Method section 8.4).

In order to access larger system sizes and evaluate the relevance of different many-body

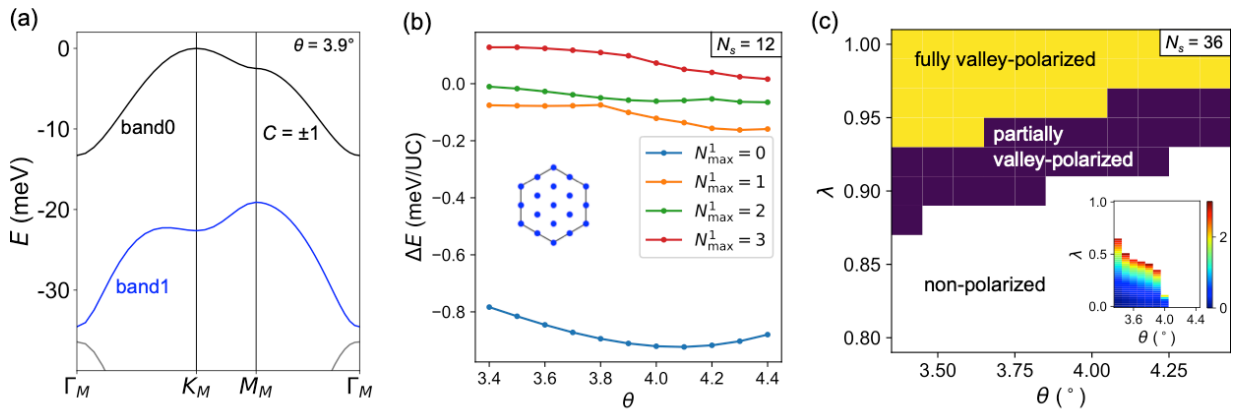


Fig. 5 Exact diagonalization calculations at $v = -4/3$. a) Continuum model band structure of the valence bands of tMoTe₂ at $\theta = 3.9^\circ$. The band closest to neutrality (band0) has valley Chern number $|C|=1$. b) Energy difference $\Delta E = E_{\text{partial}} - E_{\text{non.}}$ per unit cell between the partially valley-polarized ($v=-1, -1/3$) and non-polarized ($v = -2/3, -2/3$) sectors as a function of twist angle for the 12-site lattice (inset shows momentum mesh). The different curves correspond to the maximum number N^1_{\max} of holes allowed in the second valence band (band1). c) Ground state polarization in the variational ED calculation as a function of twist angle and intervalley interaction parameter λ for the 36-site lattice. Inset shows the FTI ratio, defined as the energy spread of the topological ground states divided by the gap. Non-white shading indicates a well-formed FTI.

phases, we implement 36-site variational ED calculations that are mostly restricted to the lowest valence band (Method section 8.3). It has been theoretically argued that mixing with higher valence bands can weaken the interaction between the valleys and induce depolarization of the system as in Fig. 5b. Here, we introduce a phenomenological tuning parameter that simply multiplies the intervalley coupling by a factor $\lambda \leq 1$. Fig. 5c shows that the ground state lies in the fully valley-polarized sector ($v_+ = -4/3$ and $v_- = 0$) for $\lambda=1$, and sequentially transitions to the PVP and non-polarized sectors as λ is reduced. The requirement of only a small suppression $\lambda \sim 0.9$ to reach the

non-polarized phase again points to the close energetic competition between distinct valley polarization sectors. Within the non-polarized sector, we do not observe signatures of a CDW at $v = -4/3$ in the numerical result. In the inset of Fig. 5c, we further assess the possibility of an FTI ground state and find that it is only present for $\theta \leq 4.0^\circ$. Interestingly, this upper limit on the twist angle, which can be traced to the stability of the valley-polarized FCI at $v = -2/3$, is similar to the threshold of the experimentally-observed AFM-like behavior. While the FTI only survives to $\lambda \sim 0.5$, we emphasize that a more definitive determination of FTI stability is highly sensitive to detailed treatment of band-mixing, screening and short-range interaction effects^{11,46}, which we defer to future studies.

In summary, we present magnetic signatures for a putative FTI in tMoTe₂ at $v = -4/3$. This interpretation is supported by ED calculations revealing the extremely small energy difference ($\Delta E < 1$ meV) between the proposed FTI ($v_+ = -2/3$, $v_- = -2/3$) and PVP states ($v_\pm = -1$, $v_\mp = -1/3$), explaining the experimental observation of small magnetic field in inducing first-order phase transitions. Recent transport measurements on tMoTe₂ confirmed the presence of a resistive state at $v = -4/3$, but it is not known if the measured longitudinal resistances are determined primarily by the FTI resistance. These results call for future experiments to precisely determine the quantized conductance of the edge modes.

METHOD

1. Device Fabrication and Characterization

Van der Waals flakes used to assemble the heterostructure devices, including graphite, h-BN, and monolayer MoTe₂, were mechanically exfoliated onto oxygen-plasma-cleaned Si/SiO₂ substrates and identified by optical contrast microscopy. Atomic force microscopy (AFM) was used to determine h-BN thickness and to verify that the flakes were free of surface residue. Owing to the air sensitivity of MoTe₂, its exfoliation and all subsequent fabrication steps were carried out in an argon-filled glovebox with H₂O and O₂ levels below 0.1 ppm. Prior to assembly, the MoTe₂ monolayer was cut into two halves using an AFM tip. Heterostructures were fabricated using standard dry-transfer techniques. The top gate was assembled first by sequentially picking up h-BN, the top graphite electrode, the top-gate h-BN dielectric, and a graphite grounding pin. One half of the MoTe₂ flake was then picked up, while the second half was rotated by the desired twist angle before being picked up and stacked to form the moiré superlattice. The completed stack was subsequently placed onto a prefabricated back gate consisting of a graphite electrode capped with an h-BN dielectric, along with gold contacts and wire-bonding pads defined by electron-beam lithography and electron-beam evaporation to enable electrical access to both gates and the grounding pin. The back-gate surface was AFM-cleaned in contact mode prior to transfer. The final heterostructure was released onto the SiO₂/Si substrate (SiO₂ thickness: 285 nm for device 3.7°, 3.3° device and 90 nm for device 3.9° and 4.0°) by melting the PC stamp at approximately 170 °C, followed by dissolution of the polymer in anhydrous chloroform for 5 min inside the glovebox. For device D 3.7°, both the top- and bottom-gate h-BN dielectrics are 35 nm thick. For device D3.9°, the top-gate and bottom-gate h-BN thicknesses are 11.3 nm and 20.4 nm. For device D4.0°, the top-gate and bottom-gate h-BN thicknesses are 30 nm and 38 nm. For device D3.3°, the top-gate and bottom-gate h-BN thicknesses are 33 nm and 37 nm respectively. Graphite electrode thicknesses were estimated from optical contrast: the top-gate graphite corresponds to approximately 2–3 graphene layers and the bottom electrode is ~10 nm thick.

Each tMoTe₂ device was mounted in a closed-cycle cryostat (Quantum Design, OptiCool), with a base temperature reading of 1.65 K on the sample mount. While all temperatures values presented above were from the sample mount readings, the actual temperatures on the sample during experiments were likely higher.

2. Determination of Carrier Density and Twist Angle

The thickness of the bottom h-BN dielectric in twisted MoTe₂ (tMoTe₂) devices was measured using atomic force microscopy. The geometrical gate capacitance per unit area was calculated as $C = \varepsilon_{\text{h-BN}}\varepsilon_0/d_{\text{h-BN}}$, where $\varepsilon_{\text{h-BN}} = 3.0$ is the dielectric constant of h-BN, ε_0 is the vacuum permittivity, and $d_{\text{h-BN}}$ is the thickness of the corresponding h-BN layer. This expression was applied independently to the top and bottom gates to obtain the top-gate (C_{tg}) and bottom-gate (C_{bg}) capacitances. The carrier density in tMoTe₂ was determined according to $n = (V_{\text{tg}}C_{\text{tg}} + V_{\text{bg}}C_{\text{bg}})/e$, where V_{tg} and V_{bg} denote the applied top- and bottom-gate voltages, respectively, and e is the elementary charge. The twist angle of each device was extracted from photoluminescence spectroscopy. In particular, the exciton resonance exhibits pronounced and reproducible changes at superlattice filling factors $\nu = \pm 1$, which were used to determine the corresponding carrier densities. The twist angle was then calculated from the measured density using $\theta = \sqrt{8n/(\sqrt{3}a_0^2)}$, where $a_0 = 3.52 \text{ \AA}$ is the lattice constant of MoTe₂.

3. Assignment of Filling Factors

The filling factor ν defines the number of holes (or electrons) per moiré superlattice site. To determine ν , we use the well-established insulating states, $\nu = 0$, $\nu = \pm 1$ and $\nu = \pm 2$ to calibrate the respective conversion factor between gate voltage ($V_g = V_{\text{tg}} + V_{\text{bg}}$) and the filling factor. We identify the gate voltages for all insulating states, determined by the static PL spectrum for each device (Extended Data Fig. 1), further confirmed by the maximum change in reflection observed in the pump–probe maps (Fig 2).

For device D1 ($\theta = 3.9^\circ$), the gate voltages corresponding $\nu = 1$ and $\nu = -1$ are determined from the PL. Using a linear fit to these points, we establish the relationship between filling factor and gate voltage. The filling factors for other insulating states within this doping range are calculated from their gate voltages and the conversion factor. We focus on the hole-doped states. For hole-doped states beyond $\nu = -1$ the gate efficiency increases; therefore, we used $\nu = -2$ and $\nu = -1$ to define the conversion relationship for $-2 < \nu < -1$ states.

We apply a similar calibration procedure for the other devices, noting that D1 is the only device to reach filling factors beyond $\nu \geq -2$. We perform the assignment for D2 ($\theta = 3.7^\circ$), by linearly

fitting the regions $-2/3 < v < 1$ and $-2/3 < v < -1$ from the PL separately to similarly account for increasing gate effectiveness at higher densities. The fractional states $v = -4/3$ and $-3/2$ are extrapolated from the linear relationship of the $-2/3 < v < -1$ region. Due to limited resolution, the conversion factors for devices D3 ($\theta = 4.0^\circ$) and D4 ($\theta = 3.3^\circ$) are determined solely from linearly fitting the region $0 < v < -1$.

4. Pump–Probe Measurements

Ultrafast pump–probe measurements were performed using femtosecond laser pulses produced by a solid-state amplifier (CARBIDE, Light Conversion) operating at a repetition rate of 400 kHz, a central wavelength of 1,050 nm, and a pulse duration of 250 fs. The laser output was divided into pump and probe paths. For the probe arm, a fraction of the fundamental beam was focused into a YAG crystal to generate a stable white-light continuum, which was spectrally filtered using a 50 nm band-pass filter centered at $\sim 1,110$ nm to span the exciton and trion resonances of MoTe₂. In the pump arm, the beam was routed through a motorized delay stage to control the pump–probe delay Δt , then focused into a second YAG crystal to produce a broadband continuum that was subsequently filtered to $1,225 \pm 50$ nm. The pump beam was modulated by an optical chopper to alternate between pump-on and pump-off conditions. Pump and probe beams were combined collinearly and focused onto the sample using a 100 \times objective with numerical aperture 0.75, yielding spot diameters of approximately 1.5 μm for the pump and 1 μm for the probe. The effective pulse duration at the sample was estimated to be ~ 200 fs from the coherent artefact in the pump–probe cross-correlation.

The same objective was used to collect the reflected signal, which was spectrally filtered to suppress residual pump light and dispersed onto an InGaAs array detector (PyLoN-IR, Princeton Instruments). Transient reflectance spectra were obtained by comparing pump-on and pump-off signals at each delay time, and the differential reflectance was calculated as $\Delta R/R = [R(\Delta t) - R]/R$, where R denotes the reflectance without pump excitation.

The pump photon energy was chosen below the optical gap of MoTe₂ to avoid direct excitation of excitons. Throughout the measurements, the pump fluence was varied from 7 to 42 $\mu\text{J cm}^{-2}$, while the probe fluence was fixed at 22 $\mu\text{J cm}^{-2}$ (Extended Data Fig. 10). The peak amplitude of the $\Delta R/R$ signal increases linearly with pump fluence, and the characteristic electronic melting and recovery dynamics are independent of fluence over this range. Unless otherwise noted, all data

presented in the main text were acquired using pump and probe fluences of $42 \mu\text{J cm}^{-2}$ and $22 \mu\text{J cm}^{-2}$, respectively.

5. Time-Resolved MCD Measurements

Time-resolved magnetic circular dichroism measurements were performed using the same pump–probe configuration described above. The pump beam conditions were kept identical, and its polarization was found not to affect the measured MCD response. A quarter-wave plate was inserted into the probe beam path to generate left- or right-handed circularly polarized probe light. For each measurement, the probe helicity was fixed while either the out-of-plane magnetic field or the sample carrier density was swept, yielding helicity-resolved maps as a function of magnetic field or doping. The MCD signal was obtained by taking the difference between the transient reflectance signals measured with left- and right-circularly polarized probe light. For magnetic-field-dependent measurements, the magnetic field was swept in both directions to account for and correct possible hysteresis effects.

6. Exciton and Attractive Polaron Oscillator Strength.

The optical spectral weight f_{AP}^{\pm} of the attractive polaron (AP) resonances in σ^{\pm} circular polarization is directly proportional to the hole density n_{\mp} in the opposite K_{\mp} valley. This proportionality enables AP resonances to serve as a direct optical probe of spin–valley polarization in twisted MoTe₂, as established in studies of exciton–polaron physics in two-dimensional semiconductors^{47,48}. Because resonant excitation of the AP transition does not involve intermediate energy relaxation processes, the circular polarization degree of the AP response,

$$\rho_{\text{AP}} = \frac{f_{\text{AP}}^- - f_{\text{AP}}^+}{f_{\text{AP}}^- + f_{\text{AP}}^+} \quad (1)$$

directly reflects the spin–valley polarization of the hole system,

$$\langle S_z \rangle = \frac{n_+ - n_-}{n_+ + n_-} \quad (2)$$

Following the formalism developed in these works, the σ^{\pm} -polarized AP transitions in moiré MoTe₂ are described by a two-dimensional complex optical susceptibility,

$$\chi_{\text{AP}}^{\pm}(E) = -\frac{\hbar c}{E_{\text{AP}}^{\pm}} \frac{\gamma_{\text{rad}}^{\pm}}{E - E_{\text{AP}}^{\pm} + i\Gamma^{\pm}/2} \quad (3)$$

where E is the photon energy, E_{AP}^{\pm} denotes the AP resonance energy, Γ^{\pm} is the total decay rate, $\Gamma^{\pm} = \frac{\gamma_{\text{rad}}^{\pm}}{\hbar} + \frac{\gamma_{\text{nrad}}^{\pm}}{\hbar}$, and $\gamma_{\text{rad}}^{\pm}/\hbar$ and $\gamma_{\text{nrad}}^{\pm}/\hbar$ are the radiative and non-radiative decay rates, respectively. The radiative decay rate is proportional to the oscillator strength f_{AP}^{\pm} and therefore encodes the valley-resolved carrier population.

The measured reflectance response is obtained by relating this two-dimensional susceptibility to the optical boundary conditions at the MoTe_2 sample. Specifically, the contribution of the AP transition to the complex reflection amplitude can be expressed as an effective sheet response by the Fresnel relation for a two-dimensional sheet,

$$r_{\text{AP}}^{\pm}(E) = -\frac{i\omega}{2c} \chi_{\text{AP}}^{\pm}(E) \quad (4)$$

with $\omega = E/\hbar$. To account for the multilayer environment of the sample, the total complex reflection amplitude is calculated using the transfer matrix method (TMM), which simulates the dielectric stack both with and without the MoTe_2 bilayer. In this framework, the entire moiré bilayer is treated as a two-dimensional conducting sheet whose optical susceptibility modifies the boundary conditions at its interface. The total reflection coefficient $R(E, \Delta t)$ in the presence of pump is obtained by inserting the sheet susceptibility into the transfer matrix of the full stack while the reference reflection coefficient $R_0(E)$ is calculated for the same stack in the absence of the sample, defining the equilibrium reflectance measured at negative pump–probe delay (before time zero), with $R = |r_{\text{AP}}^{\pm}|^2$. The differential reflectance is then evaluated as $\Delta R/R_0 = [R(E, \Delta t) - R_0(E)]/R_0(E)$.

For quantitative comparison with experiment, a smooth background contribution is included by adding a linear background term $s_{bg}(E - E_0)$ and constant offset C , accounting for residual reflectance from nearby optical transitions such as the neutral exciton or repulsive polaron, which are not explicitly included in χ_{AP}^{\pm} . In some cases, reflectance model is scaled by an amplitude term A to account for possible losses in the beam path. This treatment follows the analysis approach adopted in references^{47,48}. Extended Data Fig. 9.

7. Optical Switching Effect

Optical switching of the Chern number for integer and fractional Chern Insulators has recently been demonstrated in moiré MoTe_2 .^{23–25} We consider the possibility of resonant probe-induced

switching as an alternate explanation for the AFM-like signature. We compare the net photon fluence in our transient experiments versus the experimental conditions in which switching has been reported. Holtzmann and coworkers achieve Chern number switching by using a supercontinuum laser (50 MHz) for several seconds on the sample at an average power of 100 nW, resulting a pulse energy of 10^{-9} μ J. Assuming their beam radius on the order of $\sim\mu$ m, this corresponds to photon flux $\Phi_{\text{switch}} \sim 10^{17}$ $\text{cm}^{-2}\text{s}^{-1}$. A conservative estimate of 10 s integration to reach the switching threshold corresponds to a net photon fluence of 10^{18} photons/ cm^2 . In our experiment, the probe pulse energy is 1.5×10^{-7} μ J (from an average power $P \sim 200$ nW and a laser repetition rate 400 kHz). Since the pump-probe experiment initiates the state for every pump-probe pulse pair, the net photon fluence, 10^{14} photons/ cm^2 , on the sample is four-orders-magnitude lower than what is needed to induce switching. We conclude that resonant probe induced switching of the Chern number does not occur in our measurement.

8. Theoretical Calculations

8.1. Interacting continuum model

To theoretically study the moiré valence bands of tMoTe₂, we adopt the continuum model⁴⁹, which we briefly summarize here following the conventions of Refs.^{32,50}. Owing to strong Ising spin-orbit coupling, the low-energy valence states of tMoTe₂ are spin-valley locked, such that valley K (K') is associated with spin \uparrow (\downarrow). Henceforth, we use the term valley to refer to this spin-valley degree of freedom. We introduce a flavor index $\tau = +, -$ to label valley K^+ , K^- respectively. The continuum model for $\tau = +$ reads

$$H_{kin}^+ = \begin{pmatrix} h_b(\mathbf{r}) & t(\mathbf{r}) \\ t^*(\mathbf{r}) & h_t(\mathbf{r}) \end{pmatrix} \quad (5)$$

where the matrix structure refers to layer $l = b, t$. The non-interacting Hamiltonian for valley K' can be obtained using time-reversal symmetry. The intralayer term is

$$h_l(\mathbf{r}) = \frac{\hbar^2 \nabla^2}{2m^*} + V_l(\mathbf{r}) \quad (6)$$

where $m^* = 0.6m_e$, $(-1)^t = 1$ and $(-1)^b = -1$. The moiré potential $V_l(r)$ and interlayer hopping $t(r)$ are

$$V_l(\mathbf{r}) = V e^{(-)^l i\psi} \sum_{i=1,2,3} e^{i\mathbf{g}_i \cdot \mathbf{r}} + c.c. \quad (7)$$

$$t(\mathbf{r}) = w \sum_{i=1,2,3} e^{-i\mathbf{q}_i \cdot \mathbf{r}} \quad (8)$$

The moiré wavevectors are $\mathbf{q}_1 = \frac{8\pi \sin \frac{\theta}{2}}{3a_0} (0,1)$ and $\mathbf{q}_j = \hat{C}_3^{j-1} \mathbf{q}_1$, where $a_0 = 0.352\text{nm}$ is the lattice constant of MoTe₂ and \hat{C}_3 denotes counterclockwise rotation by $2\pi/3$. We have also defined $\mathbf{b}_j = \mathbf{q}_{j+2} - \mathbf{q}_{j+1}$. Note that we keep only the first harmonics in the moiré terms. We use the parameters $w = -18.8$ meV, $V = 16.5$ meV, $\psi = -105.9^\circ$ which were extracted from *ab initio* calculations at $\theta = 3.89^\circ$.⁵⁰ When investigating different twist angles, we will simply change θ in the continuum model while keeping the other parameters fixed, which we expect to be a reasonable approximation in the range $\theta \simeq 3.4^\circ - 4.4^\circ$.

Diagonalizing the continuum model yields moiré Bloch wavefunctions and the single-particle dispersion indexed by the band label m and the moiré momentum \mathbf{k} in the moiré Brillouin zone (mBZ). We incorporate long-range density-density interactions as

$$\hat{H}_{int} = \frac{1}{2\Omega} \sum_{\mathbf{q}} \sum_{\tau\tau'} V_{\tau\tau'}(\mathbf{q}) : \hat{\rho}_{\tau}(\mathbf{q}) \hat{\rho}_{\tau'}(-\mathbf{q}) :_{v=0} \quad (9)$$

$$\hat{\rho}_{\tau}(\mathbf{q}) = \sum_{\mathbf{k} \in mBZ} \sum_{mn} \lambda_{mn}^{\tau}(\mathbf{k}, \mathbf{q}) c_{\tau, \mathbf{k}, m}^{\dagger} c_{\tau, \mathbf{k} + \mathbf{q}, n} \quad (10)$$

$$\lambda_{mn}^{\tau}(\mathbf{k}, \mathbf{q}) = \langle u_{\mathbf{k}, m}^{\tau} | u_{\mathbf{k} + \mathbf{q}, n}^{\tau} \rangle, \quad (11)$$

where $c_{\tau, \mathbf{k}, m}^{\dagger}$ is an electron creation operator, $|u_{\mathbf{k}, m}^{\tau}\rangle$ is the cell-periodic part of the moiré Bloch function, and Ω is the system area. $: \dots :_{v=0}$ denotes normal-ordering with respect to the fully occupied valence bands — this is effectively equivalent to placing all electron creation operators to the right of annihilation operators. The interaction potential $V_{\tau\tau'}(\mathbf{q})$ used in the calculations will be specified below, though generically we have $V_{++} = V_{--}$ and $V_{+-} = V_{-+}$ due to time-reversal symmetry. The interacting continuum model consists of the non-interacting continuum model for both valleys augmented with the interaction \hat{H}_{int} . Note that the Hamiltonian satisfies a valley- $U_v(1)$ symmetry, corresponding to conservation of particle number in each valley sector.

8.2. Exact diagonalization calculations of spin polarization at $v = -4/3$

Setup. To study the energy competition between different valley polarization sectors at $v = -4/3$ in tMoTe₂, we employ exact diagonalization (ED) calculations on the interacting continuum model. Owing to the $U_v(1)$ symmetry, this can be achieved by performing calculations at different partial valley fillings v_+, v_- , where $v_+ + v_- = v = -4/3$.

For the interaction potential, we use the dual gate-screened interaction

$$V_{\tau\tau'}(\mathbf{q}) = \frac{e^2}{2\epsilon_0\epsilon_r q} \tanh \frac{q\xi}{2}, \quad (12)$$

with dielectric constant $\epsilon_r = 10$ and gate-screening parameter $\xi = 20\text{nm}$. Since $V_{\tau\tau'}(q)$ represents the ‘bare’ longrange Coulomb interaction, it is valley isotropic in that it does not depend on the valley indices τ, τ' . This is motivated from the fact that the two valleys in MoTe₂ occupy the same region in real-space.

Due to the exponential complexity of ED, it is necessary to reduce the single-particle Hilbert space, which is achieved in two ways. First, we consider small finite systems with N_s moiré unit cells. Second, we perform band truncation and restrict our attention to the lowest two valence bands per valley, which are referred to as band0 and band1 (see Extended Data Fig. 10a). This implies that all other valence bands are assumed to be fully occupied, i.e. devoid of holes. However, even for a small system with $N_s = 12$, the momentum-resolved many-body Hilbert space dimension for a two-band calculation at $\nu_+ = \nu_- = -2/3$ is $\sim 3 \times 10^{10}$, which is prohibitively large. Therefore, we further implement the ‘band-max’ truncation technique previously utilized in Refs. ^{11,51}. In the current context, this involves starting with the limit of a single-band calculation ($N_{max}^1 = 0$) where the holes are only allowed to enter band0, while band1 is fully occupied by electrons. However, it has been established from prior theoretical studies that the effects of band1 are important for capturing even qualitative aspects of the phase diagram^{44,45,50}. This is not surprising given that the indirect gap between band0 and band1 is small. To systematically approach the two-band limit, we thus perform a sequence of ED calculations where we allow at most N_{max}^1 holes to populate band1. Intuitively, this enables ‘band-mixing’ between band0 with the next valence band.

In the single-band limit, the maximum allowed polarization is the partially valley-polarized (PVP) sector where $\nu_+ = -1$ and $\nu_- = -1/3$. Therefore, in our band-mixing calculations, we focus primarily on the competition between the PVP sector and the non-polarized (NP) sector with $\nu_+ = \nu_- = -2/3$. We compute the ground state energies E_{PVP} and E_{NP} in these sectors and compare their difference as a function of twist angle and band-mixing N_{max}^1 .

Results. In Figs. 1b)-f), we plot $E_{\text{PVP}} - E_{\text{NP}}$ per unit cell as a function of $\theta \in [3.4^\circ, 4.2^\circ]$ and N_{\max}^1 for different finite lattices. Note that in order to gauge the finite-size effects, for $N_s = 12, 15$, we have used tilted lattices to generate different momentum meshes (inset) for the same N_s . These tilted lattices have more isotropic aspect ratios than their non-tilted counterparts. For all meshes considered, the PVP sector has lower energy than the NP sector in the single-band limit ($N_{\max}^1 = 0$). However, the energy difference is small, being less than 1meV per unit cell, implying a close energetic competition. As we increase N_{\max}^1 , the energy of the NP sector is lowered relative to the PVP sector. For the $N_s = 12$ meshes [see panels b) and c)], we observe that the NP sector attains a lower energy than the PVP sector, though it is possible that this also eventually occurs for the $N_s = 15$ meshes if N_{\max}^1 is pushed beyond the limit we can currently access numerically. Our results strongly suggest that band-mixing has the effect of depolarizing the system (see also Ref. [2]), though the energetic competition remains very close.

Due to finite-size effects, we do not characterize the nature of the ground state within each valley polarization sector in these small- N_s calculations. For example, even the stability of the $v = -2/3$ valley-polarized fractional Chern insulator (FCI) is sensitive to finite-size effects for such small N_s . We observe noticeable finite-size variations in the results of Extended Data Fig. 10. We are hence unable to extract a definite twist angle dependence of the spin polarization at $v = -4/3$ from Extended Data Fig. 10.

Finally, we consider the fully valley-polarized (FVP) sector ($v_+ = -4/3$ and $v_- = 0$). Note that the FVP sector necessarily involves a non-zero number of holes beyond band0, and hence cannot be accessed without band-mixing. For this reason, we are forced to restrict to the small system $N_s = 9$ where the calculation is computationally feasible across the FVP, PVP, NP sectors for sufficiently large N_{\max}^1 . Our results in Extended Data Fig. 10g) suggest that the FVP sector is less competitive than the PVP sector. We remark that a previous experimental investigation found that large magnetic fields $\sim 10\text{T}$ are required to fully valley-polarize the system at $v = -2$.²¹

8.3. Investigation of $n_s = 36$ system at $v = -4/3$

8.3.1. *Setup.*

Motivated by the finite-size effects of the unbiased ED calculations in Sec. II, we investigate a larger system size of $N_s = 6 \times 6$ in this section. Such a lattice avoids geometrical frustrations that can artificially penalize CDW states at the K_M , K_M' or M_M points. While a larger N_s is expected to reduce the finite-size

effects, it also necessitates more constraining approximations to tame the growth of the Hilbert space. For example, even a single-band ED calculation with $N_s = 36$ for the NP sector involves a many-body Hilbert space of dimension $\sim 4 \times 10^{16}$. In the following, we describe our approach to obtain ‘model-state variational’ energies in the FVP, PVP, and NP sectors for twist angles $\theta \in [3.4^\circ, 4.4^\circ]$.

8.3.2. Model-state variational calculation for the NP sector.

For the NP sector ($v_+ = v_- = -2/3$), the computational difficulty arises because holes occupy both valleys. However, a fully valley-polarized single-band calculation at $v = -2/3$ only involves a Hilbert space dimension of 3.5×10^7 , which is feasible. Furthermore, several of the candidate states at $v = -4/3$ can be adiabatically connected to a decoupled product of many-body states from the two valleys. For example, a model wavefunction for the fractional topological insulator (FTI) at $v = -4/3$ can be constructed via the decoupled product of $v_\tau = -2/3$ FCIs from the two valleys.

The above discussion motivates the following ‘model-state variational’ calculation to study the NP sector at $v = -4/3$. First, we perform a valley-polarized single-band ED calculation at $v_+ = -2/3, v_- = 0$. From this, we select some number of lowest energy many-body states $|\phi_\alpha^+\rangle$ indexed by α , with corresponding many-body energies E_α^+ . The choice of states will be discussed shortly. By time-reversal symmetry, we can obtain analogous results for $v_+ = 0, v_- = -2/3$, yielding $|\phi_\beta^-\rangle$ and E_β^- . We will refer to these selected states as ‘input states’. To address the NP sector with $v_+ = v_- = -2/3$, the idea then is to consider a variational calculation in the space of many-body states

$|\langle\alpha, \beta\rangle\rangle \equiv |\phi_\alpha^+\rangle \otimes |\phi_\beta^-\rangle$, spanned by taking products of the input states. Note that the total many-body Hamiltonian can be decomposed as

$$\hat{H} = \hat{H}^+ + \hat{H}^- + \hat{H}^{inter} \quad (13)$$

$$\hat{H}^\tau = \hat{H}_{kin}^\tau + \hat{H}_{int}^\tau \quad (14)$$

$$\hat{H}_{int}^\tau = \frac{1}{2\Omega} \sum_{\mathbf{q}} V_{\tau\tau}(\mathbf{q}) : \hat{\rho}_\tau(\mathbf{q}) \hat{\rho}_{\tau'}(-\mathbf{q}) :_{v=0} \quad (15)$$

$$\hat{H}^{inter} = \frac{1}{\Omega} \sum_{\mathbf{q}} V_{+-}(\mathbf{q}) : \hat{\rho}_+(\mathbf{q}) \hat{\rho}_-(-\mathbf{q}) :_{v=0}, \quad (16)$$

where we have used the fact that $V_{+-} = V_{-+}$. The goal is to construct the effective Hamiltonian with matrix elements

$$\tilde{H}_{(\alpha, \beta);(\alpha', \beta')} = \langle (\alpha, \beta) | \hat{H} | (\alpha', \beta') \rangle. \quad (17)$$

Clearly, we have

$$\langle(\alpha, \beta)|\hat{H}^+ + \hat{H}^-|(\alpha', \beta')\rangle = \delta_{\alpha\alpha'}\delta_{\beta\beta'}(E_\alpha^+ + E_\beta^-) \quad (18)$$

The remaining intervalley contribution $\langle(\alpha, \beta)|\hat{H}^{inter}|(\alpha', \beta')\rangle$ can be assembled via the valley-diagonal one-body correlation functions $\langle\phi_\alpha^+|\hat{\rho}_+(\mathbf{q})|\phi_{\alpha'}^+\rangle$ and $\langle\phi_\beta^-|\hat{\rho}_-(\mathbf{q})|\phi_{\beta'}^-\rangle$ of the input states.

We can then diagonalize \tilde{H} .

We now discuss the choice of input states arising from the $\nu_+ = -2/3, \nu_- = 0$ calculation. Two possibilities for incompressible phases at $\nu_+ = -2/3, \nu_- = 0$ include an FCI and charge density waves (CDW). On the 6×6 lattice, these manifest as distinct signatures in the low-energy many-body spectrum. In particular, an FCI would yield a three-fold topological degeneracy at total momentum $(k_1, k_2) = (0, 0)$ separated by a finite gap to higher states. On the other hand, a K_M -CDW corresponding to a $\sqrt{3} \times \sqrt{3}$ unit cell reconstruction would show up as three degenerate ground states at distinct momenta $(k_1, k_2) = (0, 0), (2, 2), (4, 4)$ separated by a finite gap to higher states. We choose 74 input states corresponding to the four (two) lowest states for zero (non-zero) total many-body momentum, which allows both these possibilities to appear. This means that the corresponding effective Hamiltonian H^* for the NP sector at $\nu = -4/3$ has an effective Hilbert space dimension of approximately $74^2/36 \simeq 150$ per momentum, which can be straightforwardly diagonalized. We have checked that retaining a smaller number of input states [e.g. just the 3 lowest states at $(k_1, k_2) = (0, 0)$] does not qualitatively affect the lowest energy of \tilde{H} .

In Extended Data Fig. 11a), we plot the many-body energies of the input states for the $\nu_+ = -2/3, \nu_- = 0$ calculation for some representative angles, and the interaction potential of Eq. 12 (note that the intervalley part V_+ does not matter for $\nu_+ = -2/3, \nu_- = 0$). For $3.4^\circ \leq \theta \leq 4.0^\circ$, we find clear evidence for a $\nu = -2/3$ FCI, as demonstrated by the three-fold topological degeneracy at $(k_1, k_2) = (0, 0)$. A possible candidate for an incompressible state in the NP

sector at $\nu = -4/3$ is hence an FTI. For angles greater than 4.0° , the FCI becomes destabilized. However, for the whole twist angle range studied, we do not find any evidence for a K_M -CDW or any other charge order. This is suggestive that a charge-ordered phase is not a competitive candidate in the NP sector at $\nu = -4/3$.

To further rule out the scenario of a K_M -CDW candidate in the NP sector at $\nu = -4/3$, we perform additional $\nu = -5/3$ ED calculations at $\nu_+ = -2/3, \nu_- = -1$, where the $\tau = -$ sector simply

corresponds to a fully hole-occupied band0. The rationale is that $\nu = -4/3$ is closer to $\nu = -5/3$ than $\nu = -2/3$, and the $\nu = -5/3$ calculation allows us to test whether the interaction-induced potential generated by the filled band0 in $\tau = -$ can drive CDW formation in $\tau = +$. Note that in these $\nu = -5/3$ calculations, we use the valley-isotropic interaction of Eq. 12. We find that the FCI survives for $3.4^\circ \leq \theta \leq 4.0^\circ$, and there are no signatures of K_M -CDW formation.

We defer a discussion of the intervalley interaction $V_{+-}(\mathbf{q})$ to Sec. 7.3.6, and the results of the diagonalization of \tilde{H} to Sec. 8.3.7.

8.3.3. Model-state variational calculation for the PVP sector

For the PVP sector ($\nu_+ = -1, \nu_- = -1/3$), we perform an analogous variational calculation as for the NP sector in Sec. 8.3.2. The difference is that there is only a single input state for valley K , corresponding to fully populating band0 with holes. For valley K' , we generate the input states by performing a valley-polarized single-band ED calculation at $\nu = -1/3$. Two possibilities for incompressible phases at this filling include an FCI and a K_M -CDW, which have the same signatures in the many-body spectrum as the corresponding phases at $\nu = -2/3$. Therefore, we choose 74 input states corresponding to the four (two) lowest states for zero (non-zero) total many-body momentum.

In Extended Data Fig. 11b), we plot the many-body energies of the input states for the $\nu = -1/3$ calculation for some representative angles, and the interaction potential of Eq. 12 (note that the intervalley part V_{+-} does not matter for $\nu_+ = -1/3, \nu_- = 0$). For smaller angles $\theta \leq 3.5^\circ$, we find evidence of an FCI. However, for $\theta \geq 3.7^\circ$, we instead find signatures of a K_M -CDW. This suggests that both FCI and K_M -CDW are candidate phases for the PVP sector at $\nu = -4/3$.

8.3.4. Hartree-Fock calculations allowing for IVC

The ED calculations naturally capture phases with definite valley polarization, but are not as well suited to probe states with $U_\nu(1)$ symmetry-breaking, such as intervalley-coherent (IVC) phases. To complement the ED calculations in the NP and PVP sectors, we therefore perform Hartree-Fock (HF) calculations on the same $N_s = 6 \times 6$ mesh within band0. In the HF computation, we allow for IVC at intervalley wavevectors $\mathbf{q} = \Gamma_M, K_M, K_M'$.

8.3.5. Restricted calculation for the FVP sector

While the FVP sector ($v_+ = -4/3, v_- = 0$) does not suffer from the complexity of having holes in both valleys, it does necessarily require the presence of holes beyond band0. A full two-band ED calculation in the FVP sector with $N_s = 36$ involves a Hilbert space of $\sim 2 \times 10^{17}$. To obtain a manageable calculation, we perform a restricted calculation where band0 is enforced to be fully populated with holes, and the remaining holes enter band1. This leads to a reduced Hilbert space of $\sim 3.5 \times 10^7$.

8.3.6. Intervalley interaction

We now discuss the form of the interaction used for the calculations on the $N_s = 6 \times 6$ lattice. For the intravalley interaction, we use the same dual-gate-screened form $V_{++}(q) = V_{--}(q) = \frac{e^2}{2\epsilon_0\epsilon_r q} \tanh \frac{q\xi}{2}$ with $\epsilon_r = 10$ and $\xi = 20\text{nm}$, as in Sec. 8.2. The physics of the FVP sector is not affected by the intervalley interaction. For the other calculations in this section though, the restriction to band0 means that band-mixing effects have been neglected. In Sec. 8.2., we found that a key consequence of band-mixing is the tendency to depolarize the ground state (see also Ref. ⁵⁰). To incorporate this in our band0-projected calculations in a simple manner, we introduce a parameter λ that artificially tunes the strength of the intervalley interaction according to

$$V_{+-}(q) = \lambda V_{++}(q). \quad (19)$$

As demonstrated later in Sec. 8.3.7, this will relatively lower the energy of sectors with small valley polarization. In fact, the $q = 0$ component of the intervalley interaction alone leads to an energy shift of $-\frac{V_{+-}(0)\delta N^2}{\Omega}$, where δN is the difference in number of holes between valley K and K' . Suppression of the positive quantity $V_{+-}(0)$ will therefore relatively favor the NP sector with $\delta N = 0$.

Refs.^{46,52} have previously employed second-order perturbation theory to study inter-band effects in a model consisting of Landau levels with opposite magnetic fields in the two valleys. They found that interband processes tend to weaken the intervalley interaction compared to the intravalley interaction. Ref. ¹¹ also introduced a phenomenological short-range attraction that is only operative in the intervalley channel. In the following, we will simply treat λ as a phenomenological tuning parameter and leave a more microscopic treatment to future work.

8.3.7. Results

In Extended Data Fig. 12a), we show the energy competition between the PVP and NP sectors as a function of λ and θ . We find that a suppression of the intervalley interaction ($\lambda < 1$) can lead to a transition from the PVP to the NP sector. The required intervalley suppression is quite small as the transition occurs for $\lambda \sim 0.9$ for the twist angle range studied, pointing to the close competition between the different valley polarization sectors. We note that the phase boundary moves to higher λ for larger twist angles. However, we caution that λ is a phenomenological parameter so that we refrain from making definite conclusions regarding the twist angle dependence, especially given the approximations involved in the calculations.

Extended Data Fig. 12b) shows analogous behavior for the energy competition between the FVP and NP sectors. Extended Data Fig. 12c) summarizes the ED phase diagram of the ground state polarization. Starting from the FVP sector in the valley-isotropic limit $\lambda = 1$ of the interaction, the ground state depolarizes as a function of λ until it reaches the NP sector.

In Extended Data Fig. 12d), we examine the spectrum of projected Hamiltonian \tilde{H} in the NP sector to diagnose the presence of an FTI. An FTI manifests as a 9-fold topological degenerate ground state at $(k_1, k_2) = (0, 0)$, separated by a finite gap to higher states. We define the FTI spread as the energy difference between the ninth-lowest and lowest energy states at $(k_1, k_2) = (0, 0)$. We also define the FTI gap as the energy difference between the lowest state not in this set of nine states, and the ninth-lowest energy state at $(k_1, k_2) = (0, 0)$. The FTI spread/gap is then the ratio of these two quantities and should be small for a well-formed FTI. The FTI is only present for twist angles less than 4.0° . For $\lambda = 0$, this can be understood from the fact that the two valleys are decoupled, so that the FTI is only present if the $\nu = -2/3$ calculation yields an FCI. We find that the FTI remains stable up to $\lambda \sim 0.5$. We note that the stability of the FTI is known to be highly sensitive to modelling details of both the short-range interaction (not included here) and the long-range interaction [5]. We do not find any signatures of a K_M -CDW in the NP sector.

In Extended Data Figs. 12e,f), we plot the average valley polarization $\langle S_z \rangle$ and the magnitude of IVC in the HF calculations. Recall that because the HF calculations are restricted to band0, that the maximal valley polarization is $\langle S_z \rangle = 2/3$. Similar to the ED calculations in Extended Data Fig. 12a), we find a transition between a partially polarized phase and a phase with no net polarization

for a weak intervalley suppression $\lambda \sim 0.9$. We also observe a region of IVC for moderate λ within the region of no average valley polarization. For smaller $\lambda \lesssim 0.5$, the IVC disappears (not shown).

8.4. Exact diagonalization calculations of spin polarization at $\nu = -3/2$

In this section, we follow the same approach as in Sec. 8.2, except applied to study the valley polarization at $\nu = -3/2$. Extended Data Fig. 13 shows the energy competition between the PVP ($\nu_+ = -1$ and $\nu_- = -1/2$) and NP ($\nu_+ = \nu_- = -3/4$) sectors on the $N_s = 16$ lattice. Analogous to the $\nu = -4/3$ case, we find that the PVP sector has lower energy for $N_{max}^1 = 0$. The energy difference per unit cell is smaller than at $\nu = -4/3$ (see Extended Data Fig. 10). Incorporating band-mixing relatively favors the NP sector, and we anticipate that larger N_{max}^1 may lead to the NP sector being lower energy across all twist angles. Note that the rapid growth of the Hilbert space dimension (2.1×10^5 , 1.6×10^7 , 5.4×10^8 for $N_{max}^1 = 0, 1, 2$ respectively) prevents us from studying larger N_{max}^1 . The small system size also prevents us from reliably analyzing the nature of the many-body ground state.

We note that HF calculations in the NP sector on larger system sizes can find a gapped 2×2 translation symmetry-breaking $N_s = 4 \times 4$ state, but further theoretical work is needed to fully understand the phase diagram at $\nu = -3/2$.

References

1. Cai, J. *et al.* Signatures of fractional quantum anomalous Hall states in twisted MoTe2. *Nature* **622**, 63–68 (2023).
2. Park, H. *et al.* Observation of fractionally quantized anomalous Hall effect. *Nature* **622**, 74–79 (2023).
3. Zeng, Y. *et al.* Thermodynamic evidence of fractional Chern insulator in moiré MoTe2. *Nature* **622**, 69–73 (2023).
4. Xu, F. *et al.* Observation of integer and fractional quantum anomalous Hall effects in twisted bilayer MoTe 2. *Phys. Rev. X* **13**, 031037 (2023).
5. Lu, Z. *et al.* Fractional quantum anomalous Hall effect in multilayer graphene. *Nature* **626**, 759–764 (2024).
6. Ji, Z. *et al.* Local probe of bulk and edge states in a fractional Chern insulator. *Nature* **635**, 578–583 (2024).
7. Redekop, E. *et al.* Direct magnetic imaging of fractional Chern insulators in twisted MoTe2. *Nature* **635**, 584–589 (2024).
8. Wang, Y. *et al.* Hidden states and dynamics of fractional fillings in twisted MoTe2 bilayers. *Nature* **641**, 1149–1155 (2025).

9. Park, H. *et al.* Observation of High-Temperature Dissipationless Fractional Chern Insulator. *Nat. Phys.* **s41567-025-03167-2**, (2026).
10. Xu, F. *et al.* Signatures of unconventional superconductivity near reentrant and fractional quantum anomalous Hall insulators. *arXiv preprint arXiv:2504.06972* (2025).
11. Kwan, Y. H. *et al.* Regarding the existence of abelian fractional topological insulators in twisted MoTe₂ and related systems. *Commun. Phys.* **s42005-025-02483-6**, (2026).
12. Neupert, T., Santos, L., Ryu, S., Chamon, C. & Mudry, C. Fractional topological liquids with time-reversal symmetry and their lattice realization. *Physical Review B—Condensed Matter and Materials Physics* **84**, 165107 (2011).
13. Levin, M. & Stern, A. Classification and analysis of two-dimensional Abelian fractional topological insulators. *Physical Review B—Condensed Matter and Materials Physics* **86**, 115131 (2012).
14. Repellin, C., Bernevig, B. A. & Regnault, N. Z 2 fractional topological insulators in two dimensions. *Phys. Rev. B* **90**, 245401 (2014).
15. Arseneault, E. A. *et al.* Time-domain signatures of distinct correlated insulators in a moiré superlattice. *Nat. Commun.* **16**, 549 (2025).
16. Arseneault, E. A. *et al.* Two-dimensional moiré polaronic electron crystals. *Phys. Rev. Lett.* **132**, 126501 (2024).
17. Efimkin, D. K. & MacDonald, A. H. Many-body theory of trion absorption features in two-dimensional semiconductors. *Phys. Rev. B* **95**, 035417 (2017).
18. Sidler, M. *et al.* Fermi polaron-polaritons in charge-tunable atomically thin semiconductors. *Nat. Phys.* **13**, 255–261 (2017).
19. Anderson, E. *et al.* Trion sensing of a zero-field composite Fermi liquid. *Nature* **635**, 590–595 (2024).
20. Anderson, E. *et al.* Programming correlated magnetic states with gate-controlled moiré geometry. *Science (1979)* **381**, 325–330 (2023).
21. Park, H. *et al.* Ferromagnetism and Topology of the Higher Flat Band in a Fractional Chern Insulator. *Nat. Phys.* **21**, 549–555 (2025).
22. Schmitt-Rink, S., Chemla, D. S. & Miller, D. A. B. Theory of transient excitonic optical nonlinearities in semiconductor quantum-well structures. *Phys. Rev. B* **32**, 6601 (1985).
23. Huber, O. *et al.* Optical control over topological Chern number in moiré materials. *arXiv preprint arXiv:2508.19063* (2025).
24. Holtzmann, W. *et al.* Optical Control of Integer and Fractional Chern Insulators. *arXiv preprint arXiv:2508.18639*, (2025).
25. Cai, X. *et al.* Optical Switching of Moiré Chern Ferromagnet. *arXiv preprint arXiv:2508.19602*, (2025).
26. Levin, M. & Stern, A. Fractional topological insulators. *Phys. Rev. Lett.* **103**, 196803 (2009).
27. Neupert, T., Chamon, C., Iadecola, T., Santos, L. H. & Mudry, C. Fractional (Chern and topological) insulators. *Phys. Scr.* **2015**, 014005 (2015).

28. Maciejko, J. & Fiete, G. A. Fractionalized topological insulators. *Nat. Phys.* **11**, 385–388 (2015).
29. Maciejko, J., Qi, X.-L., Karch, A. & Zhang, S.-C. Fractional topological insulators in three dimensions. *Phys. Rev. Lett.* **105**, 246809 (2010).
30. Bernevig, B. A. *et al.* Fractional quantization in insulators from Hall to Chern. *Nat. Phys.* 1–12 (2025).
31. Kang, K. *et al.* Evidence of the fractional quantum spin Hall effect in moiré MoTe2. *Nature* **628**, 522–526 (2024).
32. Yu, J. *et al.* Fractional Chern insulators versus nonmagnetic states in twisted bilayer MoTe 2. *Phys. Rev. B* **109**, 045147 (2024).
33. Zhang, Y.-H. Vortex spin liquid with neutral Fermi surface and fractional quantum spin Hall effect at odd integer filling of moiré Chern band. *Phys. Rev. Lett.* **133**, 106502 (2024).
34. Wang, C. *et al.* Higher Landau-Level Analogues and Signatures of Non-Abelian States in Twisted Bilayer MoTe 2. *Phys. Rev. Lett.* **134**, 076503 (2025).
35. May-Mann, J., Stern, A. & Devakul, T. Theory of half-integer fractional quantum spin Hall insulator edges. *Phys. Rev. B Condens. Matter Mater. Phys.* **111**, L201111 (2025).
36. Sodemann Villadiego, I. Halperin states of particles and holes in ideal time reversal invariant pairs of Chern bands and the fractional quantum spin Hall effect in moiré MoTe 2. *Phys. Rev. B* **110**, 045114 (2024).
37. Xu, C., Mao, N., Zeng, T. & Zhang, Y. Multiple Chern bands in twisted MoTe 2 and possible non-Abelian states. *Phys. Rev. Lett.* **134**, 066601 (2025).
38. Reddy, A. P., Paul, N., Abouelkomsan, A. & Fu, L. Non-Abelian fractionalization in topological minibands. *Phys. Rev. Lett.* **133**, 166503 (2024).
39. Ahn, C.-E., Lee, W., Yananose, K., Kim, Y. & Cho, G. Y. First Landau Level Physics in Second Moiré Band of Twisted Bilayer MoTe 2. *arXiv preprint arXiv:2403.19155* (2024).
40. An, L. *et al.* Observation of ferromagnetic phase in the second moiré band of twisted MoTe2. *Nat. Commun.* **16**, 5131 (2025).
41. Li, W. *et al.* Universal Magnetic Phases in Twisted Bilayer MoTe2. *Nano Lett.* (2025).
42. Muñoz-Segovia, D., Crépel, V., Queiroz, R. & Millis, A. J. Twist-angle evolution of the intervalley-coherent antiferromagnet in twisted WSe 2. *Phys. Rev. B* **112**, 085111 (2025).
43. Yu, J. *et al.* Fractional Chern insulators versus nonmagnetic states in twisted bilayer MoTe 2. *Phys. Rev. B* **109**, 045147 (2024).
44. Xu, C., Li, J., Xu, Y., Bi, Z. & Zhang, Y. Maximally localized Wannier functions, interaction models, and fractional quantum anomalous Hall effect in twisted bilayer MoTe2. *Proceedings of the National Academy of Sciences* **121**, e2316749121 (2024).
45. Abouelkomsan, A., Reddy, A. P., Fu, L. & Bergholtz, E. J. Band mixing in the quantum anomalous Hall regime of twisted semiconductor bilayers. *Phys. Rev. B* **109**, L121107 (2024).

46. Abouelkomsan, A. & Fu, L. Non-Abelian spin Hall insulator. *Phys. Rev. Res.* **7**, 023083 (2025).
47. Smoleński, T., Watanabe, K., Taniguchi, T., Kroner, M. & Imamoğlu, A. Spin-valley relaxation and exciton-induced depolarization dynamics of Landau-quantized electrons in MoSe₂ monolayer. *Phys. Rev. Lett.* **128**, 127402 (2022).
48. Scuri, G. *et al.* Large excitonic reflectivity of monolayer MoSe₂ encapsulated in hexagonal boron nitride. *Phys. Rev. Lett.* **120**, 037402 (2018).
49. Wu, F., Lovorn, T., Tutuc, E., Martin, I. & MacDonald, A. H. Topological insulators in twisted transition metal dichalcogenide homobilayers. *Phys. Rev. Lett.* **122**, 086402 (2019).
50. Jia, Y. *et al.* Moiré fractional Chern insulators. I. First-principles calculations and continuum models of twisted bilayer MoTe₂. *Phys. Rev. B* **109**, 205121 (2024).
51. Rezayi, E. H. & Simon, S. H. Breaking of Particle-Hole Symmetry by Landau Level Mixing in the $v = 5/2$ Quantized Hall State. *Phys. Rev. Lett.* **106**, 116801 (2011).
52. Xu, G., Wei, N., Villadiego, I. S. & Huang, C. Localized Excitons and Landau-Level Mixing in Time-Reversal Symmetric Pairs of Chern Bands. *arXiv preprint arXiv:2509.18438* (2025).

ACKNOWLEDGEMENTS

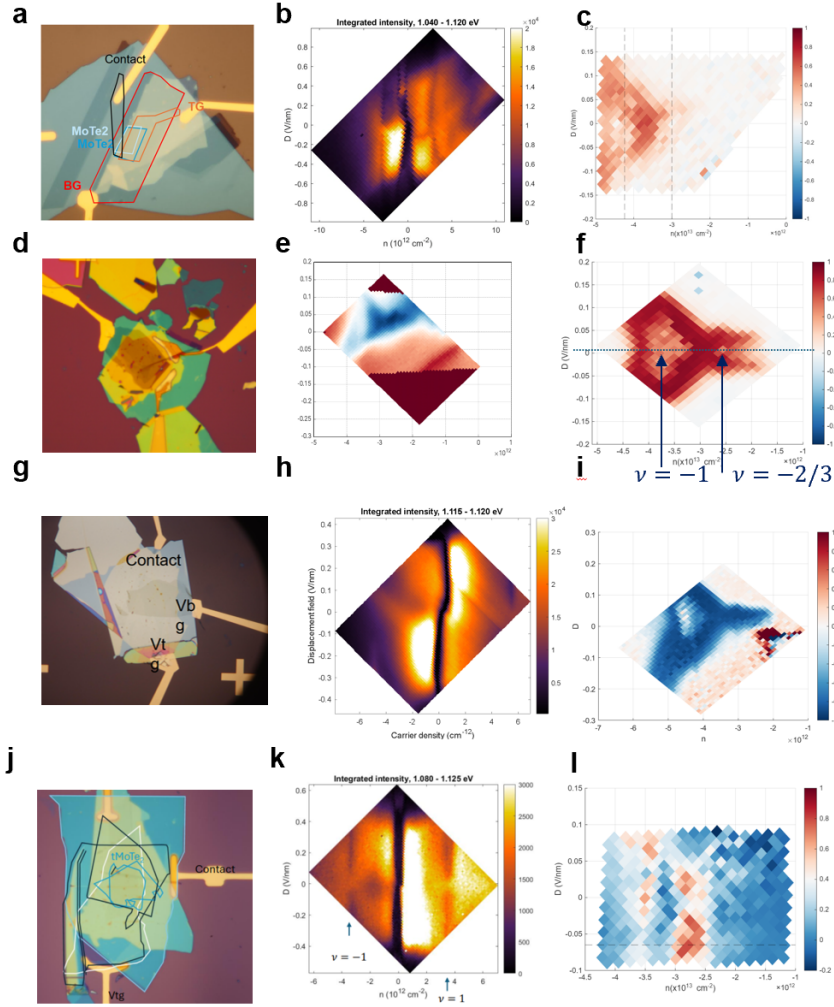
XYZ acknowledges support for GEM by the Department of Defense Multidisciplinary University Research Initiative grant number W911NF2410292 and for YW by the US Department of Energy, Office of Basic Energy Sciences (DOE-BES) under award DE-SC0024343, for the pump-probe experiments. XX acknowledges support by the U.S. Department of Energy (DOE), Office of Science, Basic Energy Sciences (BES), under the award DE-SC0018171 for the fabrication of devices D1, D3, and D4 and the Vannevar Bush Faculty Fellowship, Award number N000142512047, for the fabrication of device D2. JHC acknowledges support for the bulk MoTe₂ crystal growth and characterization and JCH acknowledges support for sample characterization, by Programmable Quantum Materials, an Energy Frontier Research Center funded by DOE BES under award DE-SC0019443. The Flatiron Institute is a division of the Simons Foundation. Additional support is acknowledged by the US Army Research Office grant number W911NF-23-1-0056 (XYZ and XR) for partial support of the experimental setup. K.W. and T.T. acknowledge support from the JSPS KAKENHI (Grant Numbers 21H05233 and 23H02052) and World Premier International Research Center Initiative (WPI), MEXT, Japan.

Author Contributions

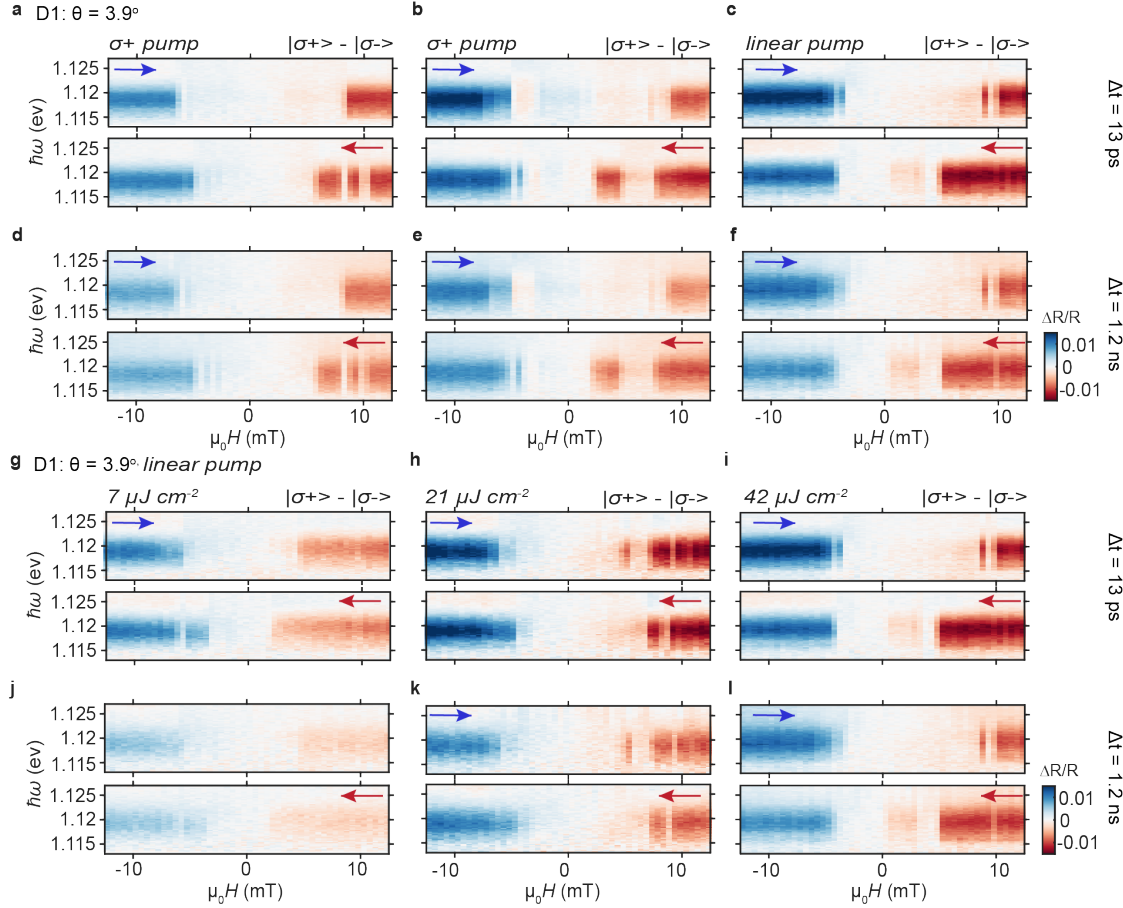
X.Y.Z., X.X., Y.W., and G.E.M. conceived this work. Y.W. and G.E.M. conducted all spectroscopic measurements, analyzed, and interpreted the results, with the assistance of J.C. under the supervision of X.Y.Z. and X.R. Sample fabrication was carried out by W.L., S.Y., E. A., C. H. under the supervision of X.X. Y.K. and N.R. carried out all theoretical calculations and simulations. J.H.C. was responsible for MoTe₂ crystal growth. T.T. and K.W. provided the hBN crystal. J.I. contributed to the interpretation of optical selection rules, under the supervision of X.Y.Z. and R.Q. J. C.H. advised on sample preparation and characterization. The manuscript was prepared by Y.W., G. E.M., X.Y.Z., X.X., N.R. and Y.K., incorporating inputs from all coauthors. X.Y.Z. supervised the project. All authors read and commented on the manuscript.

Competing Interests. The authors declare no competing interests.

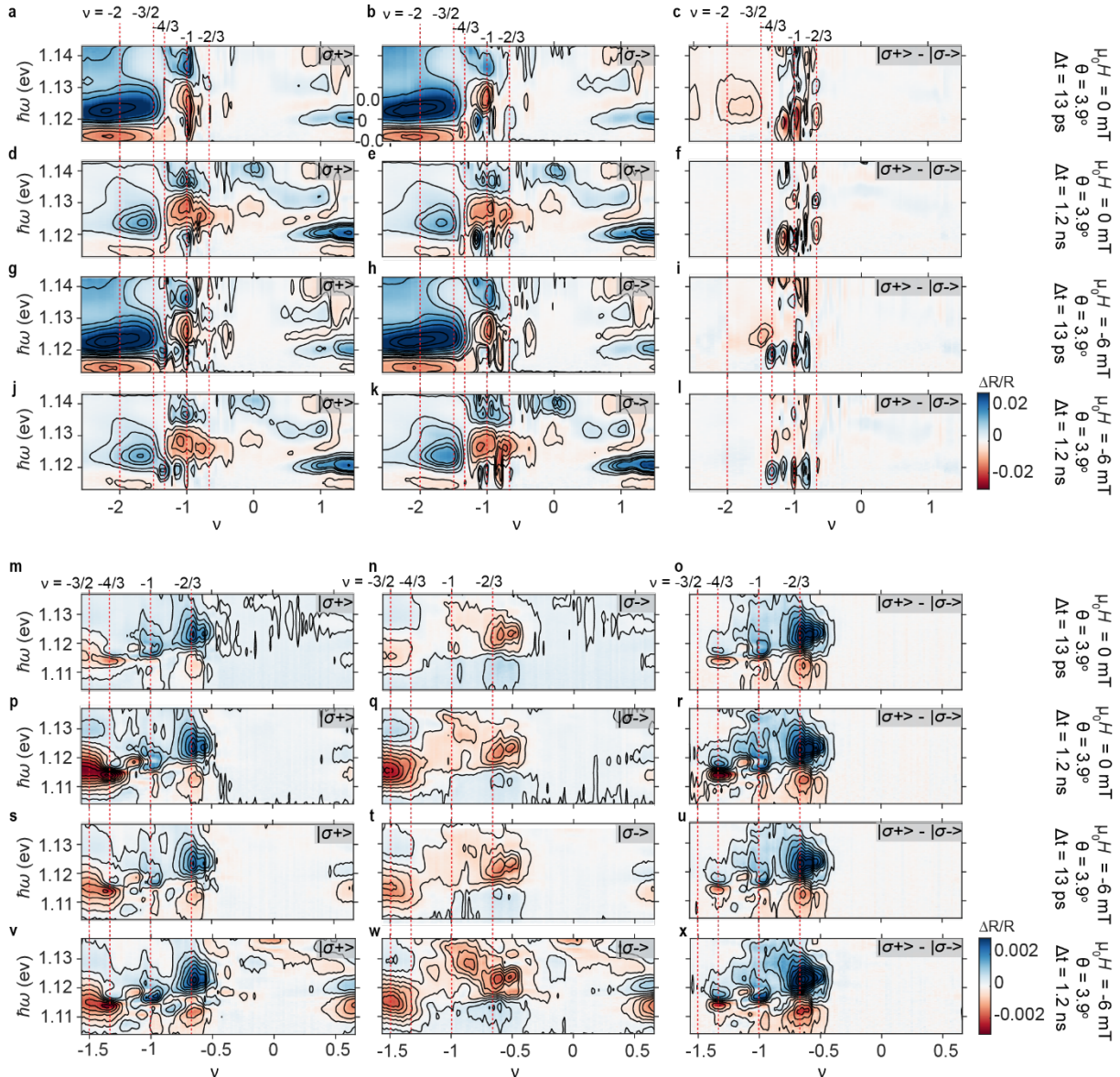
Data Availability Statement. The data shown in the main figures are available in Source Data. Data supporting the findings of this study are available from the corresponding author upon request.



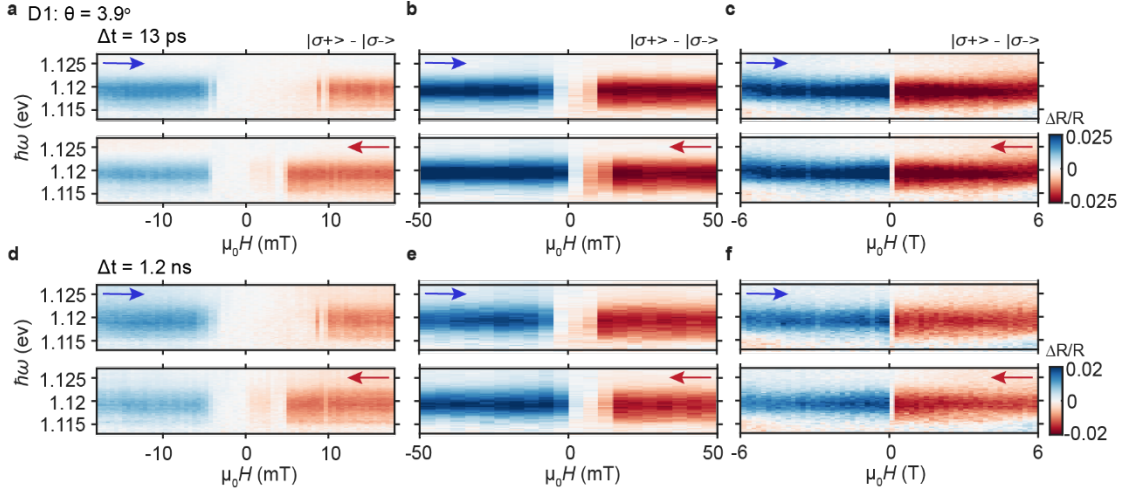
Extended Data Fig 1. Device images and characterization. a-c) D1 ($\theta = 3.9^\circ$), d-f) D2 ($\theta = 3.7^\circ$), g-i) D3 ($\theta = 4.0^\circ$), and j-l) D4 ($\theta = 3.3^\circ$). The first column presents optical images of the devices. The second column presents the trion PL for each device as a function of carrier density (n) and displacement field (D). The third column shows the n -and D -resolved degree of circular polarization, $\rho = \frac{PL(\sigma^+) - PL(\sigma^-)}{PL(\sigma^+) + PL(\sigma^-)}$. Integer and Red ($\rho \sim 1$) corresponds to the ferromagnetic region. Fractional Chern insulating states at $\nu = -1$ and $\nu = -2/3$ are indicated by a reduction in ρ contrast, and are used to calibrate the filling factor in the transient reflectance maps (Fig. 2, Extended Data Figs. 3, 7).



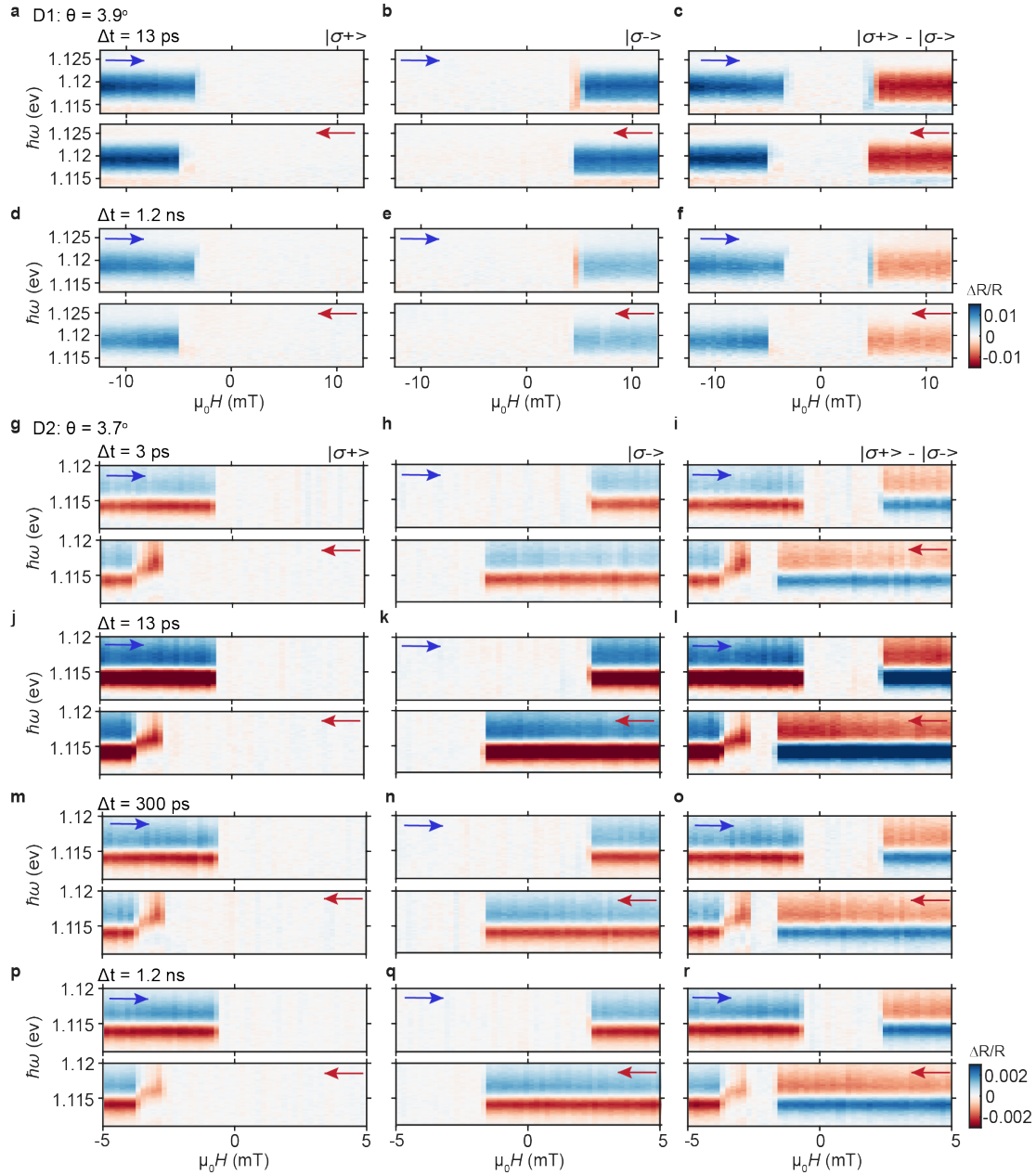
Extended Data Fig 2. Pump polarization and fluence controls. a-f Spectrally-resolved CD color maps ($\square^+ - \square^-$) for the forward (top) and reverse (bottom) sweeping magnetic field with varying pump polarization at time delays 13 ps (a-c) and 1.2ns (d-f). a,d) and b,e) present two separate magnetic field cycles, both using σ^+ -polarized pump, while c-f) are with linear-polarized pump. All data shown in (a-f) were acquired with a pump fluence of $42 \mu\text{J cm}^{-2}$. g-l CD color maps ($\square^+ - \square^-$) for the forward and reverse sweeping magnetic field with varying linear pump fluence at time delays 13 ps (g-i) and 1.2ns (j-l). Signal fluctuations are stochastic while critical fields remain similar across repeated scans, consistent with the instability of the non-polarized $v=-4/3$ phase. Signal appears independent of whether linear vs circular polarized near-IR pump ($\sim 1220\text{nm}$) is used.



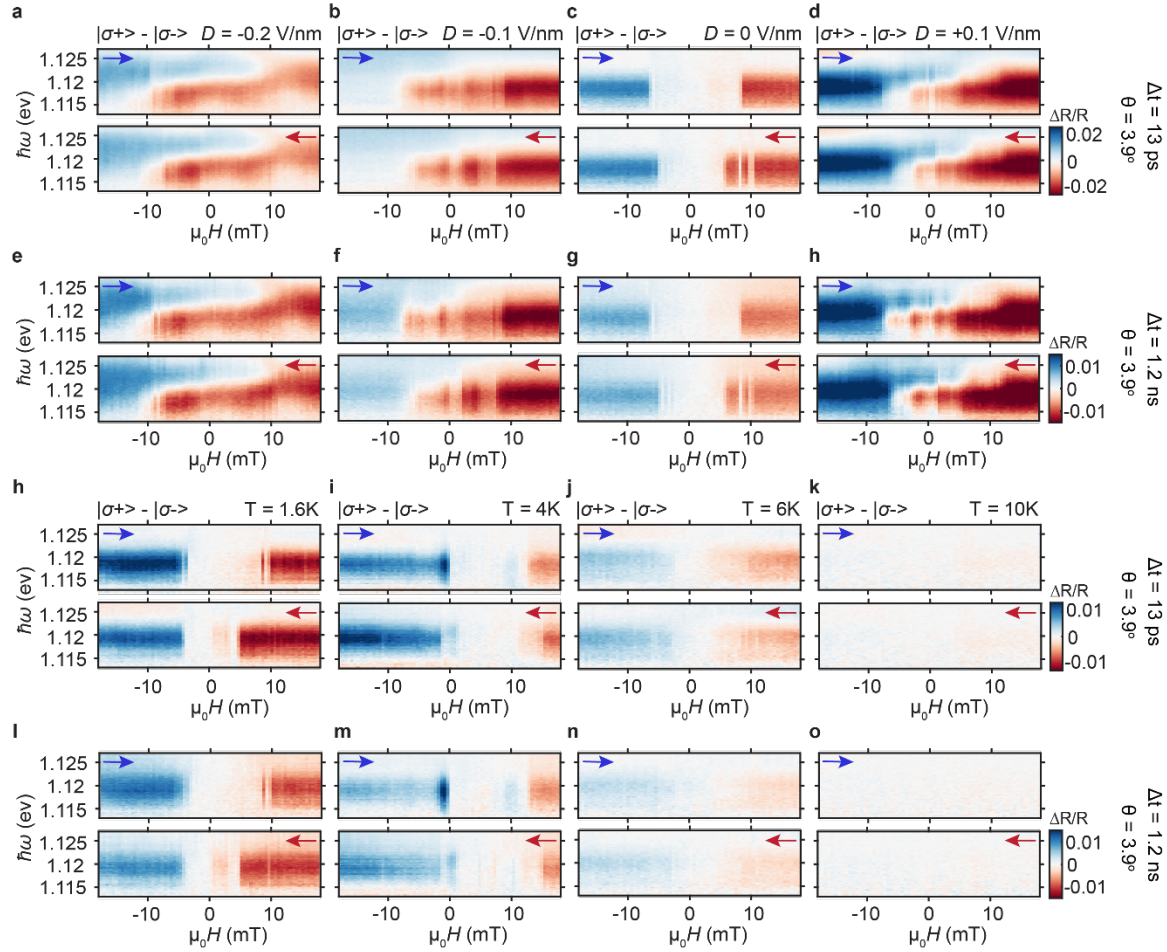
Extended Data Fig 3. Transient circular dichroism (CD) gate maps at all time delays for D1 ($\theta=3.9^\circ$) and D2 ($\theta=3.7^\circ$). Spectrally resolved transient reflectance maps as a function of moiré filling factor (n) for tMoTe₂ devices D1 ($q = 3.9^\circ$, **a-f**) and D2 ($q = 3.7^\circ$, **m-x**). The left and middle columns are $\Delta R/R$ spectra obtained with probe polarizations of $s+$ and $s-$, respectively, while the right column presents the difference spectra between the two probe polarizations ($\sigma+ - \sigma-$) as a proxy to CD signal. For D1 ($q = 3.9^\circ$, **a-f**), data were taken at $\Delta t = 13$ ps and 1.2 ns at magnetic fields 0 mT and 6 mT. The complete gatemap is shown, covering a larger doping range shown in the main text. For D2 ($q = 3.7^\circ$, **m-x**), the dynamics are shown at time delays $t = 3$ ps (**m-o**), 13 ps (**p-r**), 300 ps (**s-u**), and 1.2 ns (**v-x**). The red-dashed lines mark filling factors for $n = -2, -3/2, -4/3, -1$, and $-2/3$. All data taken at $D_{\text{eff}} = 0$ V/nm and 1.6K.



Extended Data Fig 4. Mapping the high-field phase diagram for $\nu = -\frac{4}{3}$ in D1 ($\theta = 3.9^\circ$). High field dependence of $\nu = -4/3$ at delay times a-c 13 ps and d-f 1.2 ns. The three columns present the difference spectra between the two probe polarizations $\sigma^+ - \sigma^-$ as a proxy to CD over a different magnetic field range with different step sizes. The first column (a,d) shows forward and reverse sweeps over ± 18 mT with a step size of 0.5 mT. Barring spin fluctuations, switching events occur $\leq |10|$ mT. The second column (b,e) shows magnetic field dependence over ± 50 mT with a larger step size of 5 mT, and the third (c,f) over ± 6 T with a step size of 0.2 T. Importantly, only a single switching event occurs in either direction $\leq \pm |150|$ mT. The valley polarized state is stable throughout the measured range, with a small Zeeman shift nearing ± 6 T. This observation rules out a second phase transition to a Zeeman-induced band crossing state, where $\nu = -4/3$ resides in one valley and fills the second Chern band. Note that spin fluctuations, consistent with the fragile $\nu = -4/3$ unpolarized phase, lead to variations in intensity and the precise switching field across different scans. All data taken at 1.6K, D = V/nm.

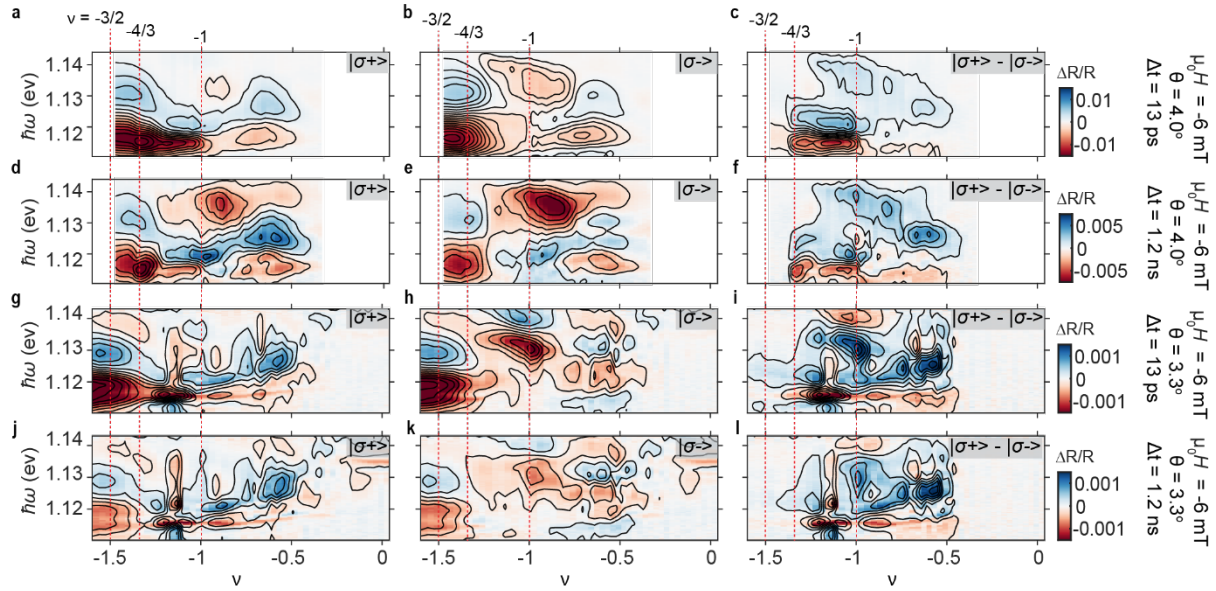


Extended Data Fig 5. First order spin-flip transition occurs at same fields at different time delays. Spectrally-resolved magnetic field dependence of AP feature in D1 ($\theta = 3.9^\circ$) (a-f) and D2 ($\theta = 3.7^\circ$) (g-r), respectively. The first column probes K with σ^+ -polarized light, the second column probes K' with σ^- -polarized light, and the third shows the difference $\sigma^+ - \sigma^-$, serving as a proxy for CD. For each device, first-order spin flip transitions persist at all measured time delays with identical switching fields (< 10 mT), differing only in intensity due to melting/recovery dynamics. Note that both devices exhibit three regions which remain flat with respect to magnetic field, including two magnetic regions and one non-magnetic region near 0 mT.

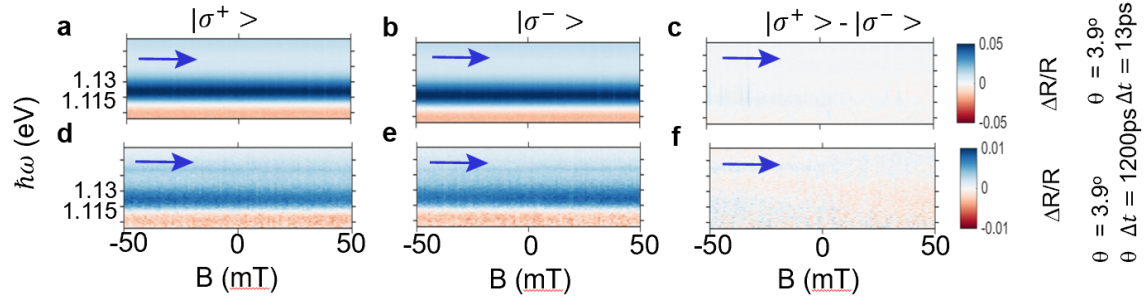


Extended Data Fig 6. Robustness of $v = -4/3$ in D1 ($\theta = 3.9^\circ$) to Displacement-field and temperature.

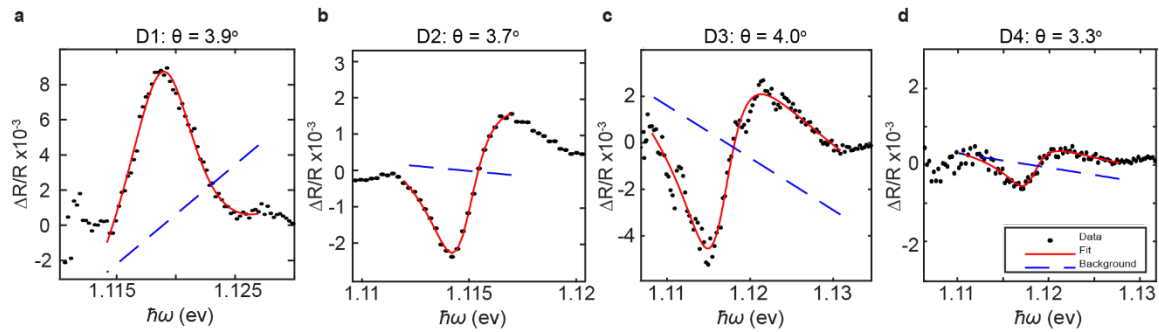
(a-h) magnetic field dependence of σ^+ - σ^- signal sweeping in forward and reverse direction as a function of displacement field (i-p) and temperature at time delays of 13 ps and 1.2 ns.



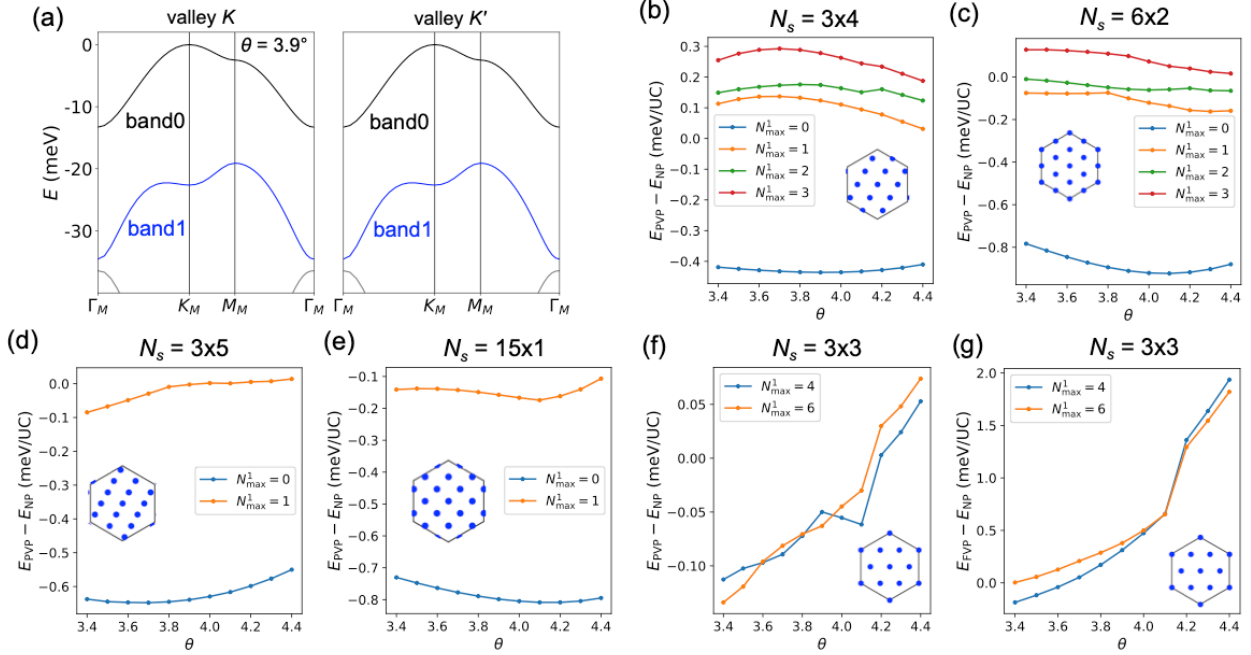
Extended Data Fig 7. Gate maps and magnetic field dependence of other twist angles (D3 $\theta = 4.0^\circ$) and (D4 $\theta = 3.3^\circ$) Spectrally-resolved gate maps as a function of filling factor on the hole-doped side. The first column shows σ^+ -polarized light, the second column shows signal probed by σ^- -polarized light, and the third column shows the difference (CD) for (a-f) D3 and (g-l) D4. Red dotted lines indicate states at $\nu = -3/2$, $-4/3$, and -1 .



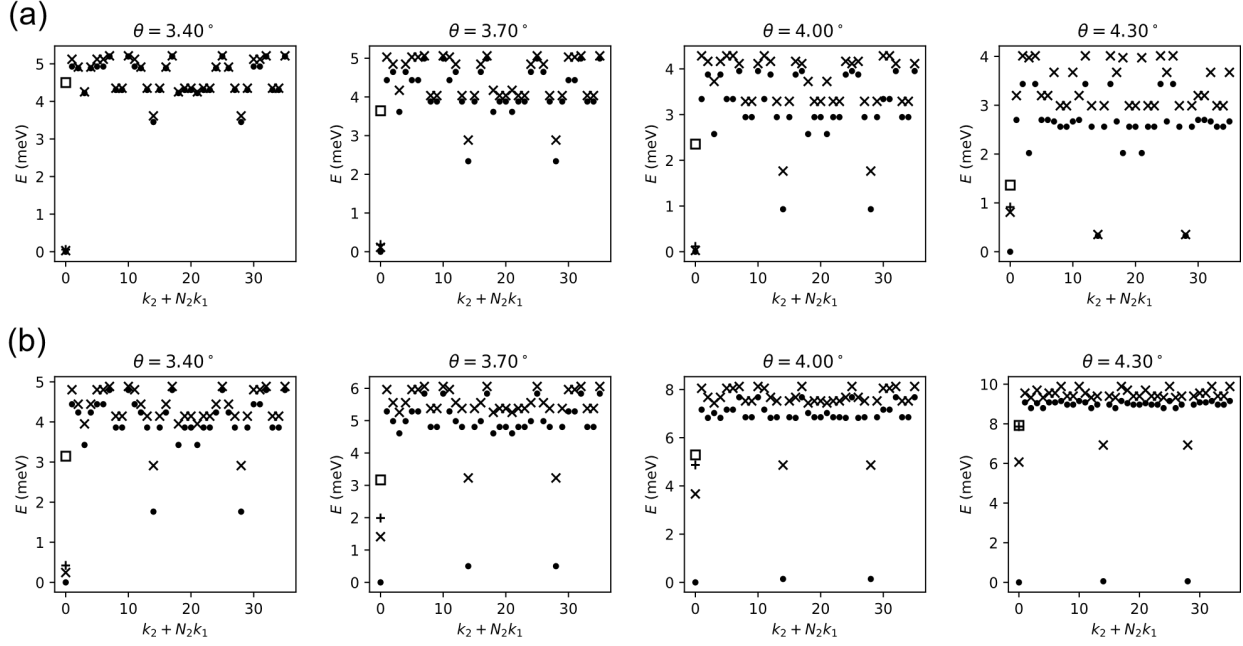
Extended Data Fig 8. Magnetic field dependence of $\nu = -2$ in D1 ($\theta = 3.9\text{deg}$), $-50\text{mT} \rightarrow +50\text{ mT}$ (raw data, no bg correction). The first column shows signal probed by σ^+ -polarized light, the second column shows signal probed by σ^- -polarized light, and the third column shows the difference (CD). The $\Delta R/R$ signal is completely flat in the measured range $\pm 50\text{mT}$, consistent with a robust non-polarized state at a filling factor of $\nu = -2$.



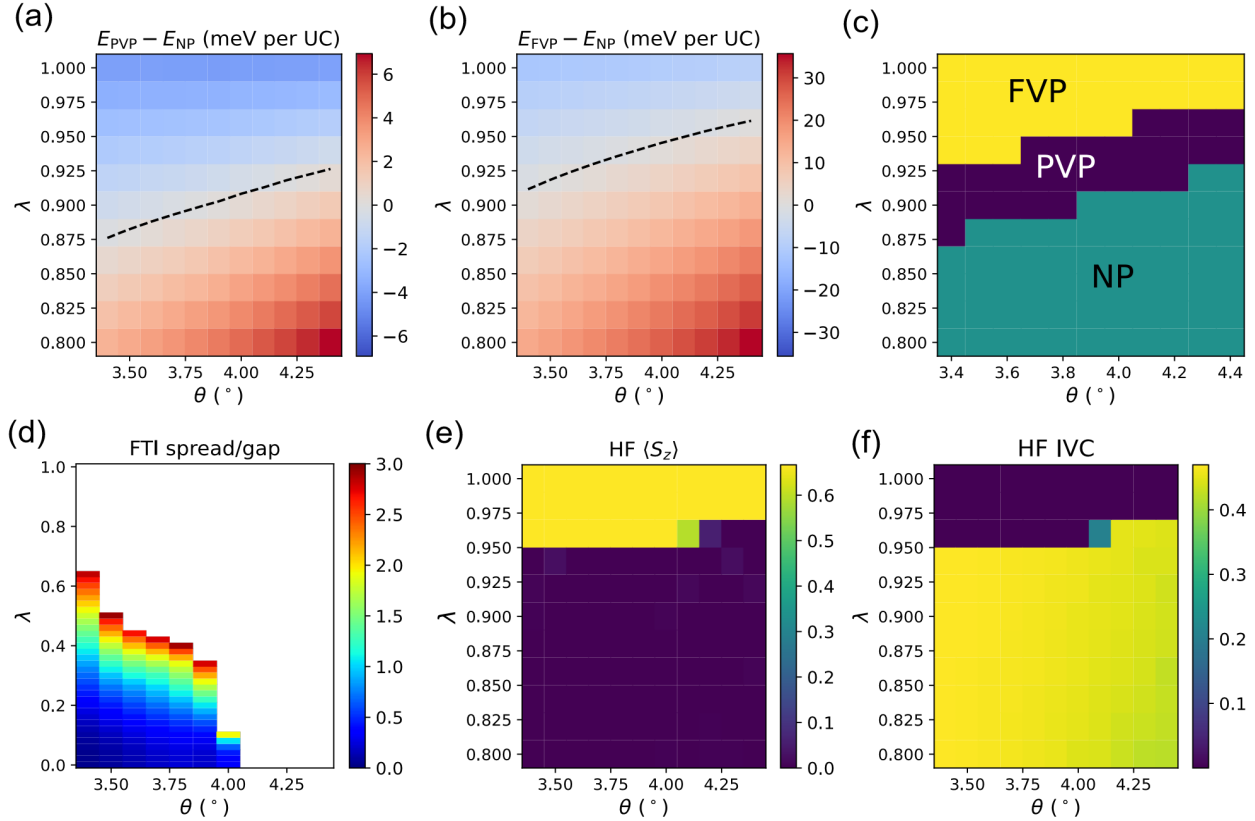
Extended Data Fig 9. Fitting $\Delta R/R$ for AP signal in the four measured devices. Sample fits of spectral cuts where there is RMCD signal at a time delay of 1200 ps. See methods for details.



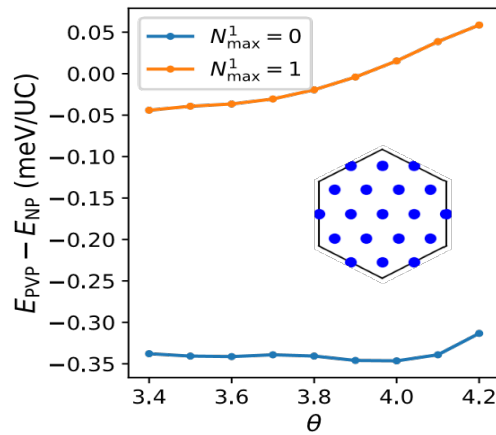
Extended Data Fig 10. Band-mixing exact diagonalization calculations of valley polarization at $\nu = -4/3$. a) Band structure of tMoTe₂ at $\theta = 3.9^\circ$ for the two valleys. The two lowest moiré valence bands are labelled as band0 and band1. b)-f) Energy difference per unit cell between the partially valley-polarized (PVP) sector ($\nu_+ = -1$ and $\nu_- = -1/3$) and the non-polarized (NP) sector ($\nu_+ = \nu_- = -2/3$) for different twist angles θ and band-mixing parameters N_{max}^1 . The panels refer to different system sizes N_s . The mBZ momentum mesh is shown as inset. g) Energy difference per unit cell between the fully valley-polarized (FVP) sector ($\nu_+ = -4/3$ and $\nu_- = 0$) and the NP sector for $N_s = 3 \times 3$.



Extended Data Fig 11. Single-band exact diagonalization calculations of fully valley-polarized states for $N_s = 6 \times 6$. a) Many-body spectra for $v_+ = -2/3, v_- = 0$. A $v = -2/3$ FCI is characterized by a topological three-fold degenerate gapped ground state at $(k_1, k_2) = (0, 0)$. For a given many-body momentum, the symbols cycle between $\cdot, \times, +, \square$ to help distinguish nearly-degenerate states. b) Same as a) except for $v_+ = -1/3, v_- = 0$. A $v = -1/3$ FCI is characterized by a topological three-fold degenerate gapped ground state at $(k_1, k_2) = (0, 0)$. A $v = -1/3$ K_M -CDW is characterized by three degenerate gapped ground states at momenta $(k_1, k_2) = (0, 0), (2, 2), (4, 4)$.



Extended Data Fig 12. Calculations at $\nu = -4/3$ for $N_s = 6 \times 6$. a) Comparison of PVP (see Sec. 8.3.3) and NP (see Sec. 8.3.2) energies, as a function of intervalley parameter λ and twist angle θ . b) Comparison of FVP (see Sec. 8.3.5) and NP energies. c) Phase diagram showing the favored polarization sector in the ED calculations. d) FTI spread/gap ratio for the NP sector. e) Average valley polarization $\langle S_z \rangle$ in the HF calculation. f) Magnitude of IVC in the HF calculation.



Extended Data Fig 13. Band-mixing exact diagonalization calculations of valley polarization at $\nu = -3/2$. Energy difference per unit cell between the partially valley-polarized (PVP) sector ($\nu_+ = -1$ and $\nu_- = -1/2$) and the non-polarized (NP) sector ($\nu_+ = \nu_- = -3/4$) for different twist angles θ and band-mixing parameters N_{max}^1 . The mBZ momentum mesh is shown as inset.